MEMS Corner Cube Retroreflectors for Free-Space Optical Communications

V.S. Hsu, J.M. Kahn, and K.S.J. Pister

Department of Electrical Engineering and Computer Sciences
514 Cory Hall
University of California
Berkeley, CA 94720

Phone: (510) 643-8848
Facsimile: (510) 642-2739
Internet: {vhsu, jmk, pister}@eecs.berkeley.edu

November 4, 1999

Abstract:

Micromachined corner cube retroreflectors (CCRs) are devices that can be employed as transmitters in wireless free-space optical communication systems. Their low power consumption, small size, and easy operation make them an attractive option in designing an optical link. A method to predict the performance of CCRs with ideal or non-ideal characteristics has been developed. Results from simulation help to determine the tolerances on mirror curvature and misalignment. The design of CCRs to be fabricated in a foundry MEMS process is discussed, and the design parameters that determine the optical, electrical and mechanical characteristics of the CCR are presented. Thus far, the CCRs that have been fabricated and tested can transmit detectable signals, but the mirror curvature and misalignment in the CCRs result in performance far from the theoretical limit.

CONTENTS

I. Introduction

Wireless communication systems are generating significant interest because they provide increased mobility and a means to create communication links where wired links cannot be made. Today, both RF and optical links are being employed in numerous applications. The choice of whether to use an RF link or optical link depends greatly on the specific application. New technologies to increase the performance of both links continue to develop. A device call the corner cube retroreflector has been introduced as a transmitter in a free-space optical communication system. This device offers extremely low power consumption (< 1 μJ/bit), it is simple to operate, and can be fabricated to sizes less than a cubic millimeter in a MEMS process.

Early attempts to fabricate CCRs in a MEMS process failed to demonstrate communication due to poor alignment, low reflectance, and low fabrication yield [13]. However, Patrick Chu at UCLA reported fabricating CCRs in a commercial MEMS process called MCNC MUMPS that were able to transmit data [14]. The results were promising and prompted further research in employing CCRs for an optical communications link.

This paper reports a study of MEMS CCRs as optical transmitters. It provides a method for predicting the performance of an ideal CCR as well as one with non-ideal characteristics. This allows the designer to determine specifications for the CCRs in order to meet the system requirements. This paper also presents the design issues relevant to fabricating CCRs in the commercial MCNC MUMPS process. The design for the current MEMS CCR is described. This design was fabricated and tested for mirror curvature, mirror misalignment, drive voltage, and rise and fall times. Methods to improve the design and performance of the CCRs are determined.

II. Free-Space Optical Communication Using a CCR

In this section, the corner cube retroreflector and its properties are defined. A free-space optical communication link employing the CCR is described, and the CCR characteristics relevant to the communication system are presented.

A. Ideal Corner Cube Retroreflectors

1. Definition

A corner cube retroreflector (CCR) is a device made up of three mutually orthogonal reflective surfaces, or mirrors, forming a concave corner. A ray of light entering a CCR is reflected back in the direction of the incident light if it hits the CCR within a particular area defined by the incident direction. By tilting and realigning a mirror or mirrors of the CCR, light can be intermittently reflected back in the direction of the interrogating light source, thereby transmitting a digital signal.

2. MEMS CCR

MEMS (Micro Electro-Mechanical Systems) technology has provided the means to fabricate very small CCRs (mirrors that are fractions of a millimeter on a side) with moveable mirrors. The mirrors can be fabricated in a MEMS process and assembled, or raised out of the substrate plane, to form a CCR. A mirror or mirrors can be actuated in a variety of ways. The design employed in this study uses electrostatic force to pull a mirror, misaligned in its starting position, into the aligned position. The return force from a flexed polysilicon beam or beams brings the mirror back to its misaligned position once the electrostatic force is removed. MEMS technology is well-suited for making very small actuating CCRs. Unfortunately, fabrication and assembly yields some misalignment and curvature in the mirrors that are a detriment to the optical performance of the CCRs.

3. Geometry

The geometry of the corner cube is such that any incident ray with direction $-\hat{\boldsymbol{n}}_i$ that strikes all three mirrors before leaving the CCR will be reflected back in the direction of the incident ray $\hat{\boldsymbol{n}}_i$. There are also two boundary cases where an incident ray can strike the CCR only once or twice and be returned to the source. The single reflection case occurs when an incident ray is normal to a mirror. The double reflection case occurs when an incident ray is parallel to one mirror surface and not normal to either of the other mirrors. Both the three reflection case and the double reflection case depend on $-\hat{\boldsymbol{n}}_i$ and where the ray initially strikes the CCR. Unless otherwise mentioned, this paper deals only with the three reflection case.

Fig. 1 shows how the direction of an incident ray along $-\hat{\boldsymbol{n}}_i$ changes direction as it propagates through a CCR. Placing the CCR in the coordinate system such that the mirrors are normal to each axis as shown in Fig. 1, the reflected direction is simply the incident direction with a change of sign on the component normal to the incident mirror.

4. Effective Area and Scattering Cross Section

As mentioned above, not all rays that strike the CCR will be reflected back in the direction of the light source. This depends on the incident direction $-\hat{\boldsymbol{n}}_i$ and the location on the CCR that the ray first makes contact. For a given $-\hat{\boldsymbol{n}}_i$, the effective area on each mirror face where an incident ray would be reflected back to the source can be determined. Fig. 2 shows how the effective area can be found for each of the six different possible cases for $-\hat{\boldsymbol{n}}_i$ for the mirror in the *xy*-plane. This can be used to find the effective area on each mirror of the CCR. For CCRs with mirror sides of length l, simply scale by l^2.

The scattering cross section $\sigma(\hat{\boldsymbol{n}}_i)$ of the CCR can be found by summing the effective areas of each mirror face scaled by the appropriate direction cosines. For the CCR in Fig. 3, the scattering cross section is found with the following expression.

$$\sigma(\hat{\boldsymbol{n}}_i) = \hat{\boldsymbol{n}}_{ix}A_1 + \hat{\boldsymbol{n}}_{iy}A_2 + \hat{\boldsymbol{n}}_{iz}A_3 \quad \textbf{(1)}$$

When the rays strike a CCR along its body diagonal, all the rays will reflect three times and be returned to the source resulting in a scattering cross section (for a CCR with mirrors each having an area A) $\sigma\left(\hat{\boldsymbol{n}}_i = \frac{1}{\sqrt{3}}(1, 1, 1)\right) = A\sqrt{3}$.

The scattering cross section of the CCR is the same for six different incident directions (Fig. 4). The vectors formed from the dots on the unit sphere to the origin represent the six incident directions that yield the same scattering cross section. In other words, a CCR has three-fold rotational symmetry about the body diagonal where the three planes of mirror symmetry are defined by the intersection of the body diagonal with the *x,y,z* axes.

B. Transmission using CCRs

Corner cube retroreflectors can be used to transmit an optical signal. To do so, the CCR must be able to direct reflected light to and away from the imaging receiver (Fig. 5). By tilting a single mirror of the CCR an angle δ, the direction of the outgoing rays will be offset. If δ is large enough, the reflected light can be directed away from the imaging receiver. A signal can be transmitted by modulating the position of a mirror from the aligned position to this tilted position. A method to approximate the minimum δ required for communication will be presented.

The interrogation path and the receive path coiincide in this communication system. A method must be designed to separate the outgoing light and the incoming light. One solution is to separate the incoming and outgoing light by their polarization. Fig. 6 depicts this method. The light from the laser is linearly polarized to pass through the polarized beam splitter. It then passes through a quarter-waveplate that changes the linear polarization of the light to circular. After three reflections off the CCR, the light returns with the opposite circular polarization. Passing through the 1/4 waveplate changes the light to the linear polarization orthogonal to the original light from the laser. This light is then reflected by the beam splitter and collected by the imaging receiver. In this setup, the position of the interrogating laser and the receiver can also be interchanged.

C. Characteristics relevant for communication

The characteristics of the CCR relevant to the communication system include the power received by the imager, the complexity of design, and the frequency at which data can be transmitted.

1. Optical

The power received by the imager can be determined from the differential scattering cross section (DSCS) $d\sigma(\hat{\boldsymbol{n}}_i, \hat{\boldsymbol{n}}_o)/d\Omega_o$ ((W/sr)/(W/m^2) or m^2/sr). The DSCS is the scattered power per unit solid angle of the observation per unit illumination irradiance. It is a function of the incident direction $-\hat{\boldsymbol{n}}_i$ and the observation direction $\hat{\boldsymbol{n}}_o$. The DSCS can be used to calculate the power received by the imager P_{rec} given the irradiance of the interrogating light source at the CCR I_i, the reflectance of the mirrors r, the diameter of the imaging lens d_{lens}, and the distance from the CCR to the imager R. As shown in Fig. 7, the lens diameter and distance determine the solid angle subtended by the receiver which is given by:

$$\Omega_0 = 2\pi\left(1 - \frac{R}{\sqrt{R^2 + \frac{d_{lens}^2}{4}}}\right) \tag{2}$$

$$P_{rec} = I_i r^3 \int_{\Omega_0} \frac{d\sigma(\hat{\boldsymbol{n}}_i, \hat{\boldsymbol{n}}_o)}{d\Omega_o}\, d\Omega_o \tag{3}$$

Note that the reflectance is cubed because the ray reflects off three mirrors.

The peak differential scattering cross section, PDSCS, is defined as the value of $d\sigma(\hat{\boldsymbol{n}}_i, \hat{\boldsymbol{n}}_o)/d\Omega_o$ along the axis of interrogation, $\hat{\boldsymbol{n}}_o = \hat{\boldsymbol{n}}_i$, regardless of whether the $d\sigma(\hat{\boldsymbol{n}}_i, \hat{\boldsymbol{n}}_o)/d\Omega_o$ is largest for $\hat{\boldsymbol{n}}_o = \hat{\boldsymbol{n}}_i$. The PDSCS is relevant because if the CCR is interrogated from a sufficiently large distance, the imager lens subtends only a small solid angle surrounding the axis of interrogation. In this case, the DSCS over the entire subtended solid angle can be approximated as the PDSCS. Therefore, the power received can be calculated approximately as follows.

$$P_{rec} \approx I_i r^3 \cdot \frac{d\sigma(\hat{\boldsymbol{n}}_i, \hat{\boldsymbol{n}}_i)}{d\Omega_o} \cdot \Omega_o \tag{4}$$

The CCR properties that affect the power received by the imager include the reflectance of the mirrors, the size of the mirrors, and the nonflatness of the mirrors. A method for finding the DSCS for CCRs with flat and nonflat mirrors will be presented in Section III.A.

2. Electrical and Mechanical

As mentioned earlier, electrostatic force is used to actuate the tilting mirror in the current design for the CCR. The voltage required to actuate the mirror to its aligned position should be minimized to simplify the requirements for the circuitry designed to drive the CCR. The characteristics of the actuating mirror that affect

the drive voltage are the size of the actuating mirror, its distance from the ground plane, its angular tilt, and the rigidity of the beam(s) supporting the mirror.

The large signal turn-on and turn-off characteristics of the CCR also depend on the size of the mirror and the rigidity of the support beam(s). The rate at which the CCR signal can be deflected to and away from the imaging receiver limits the bit rate at which the communication link can operate.

III. Optical Modeling of MEMS CCRs

The DSCS can be predicted for MEMS CCRs with ideal or non-ideal mirrors. Being able to predict the DSCS will assist in determining the mirror size, mirror reflectance, mirror flatness, and mirror alignment needed for a typical application. In addition, the directions over which a CCR can be interrogated and transmit a detectable signal can also be determined.

A. Calculating the DSCS for ideal and non-ideal CCRs

Diffractive spreading of the reflected beam puts a fundamental limit on the performance of a long-range optical link using this device. In order to model nonflatness, misalignment and diffraction on an equal footing, a finite-element analysis of the device is performed.

To begin the analysis, each face of the CCR is represented by an equation describing the surface. The CCR faces are bounded by the planes $x = 0$, $x = l$, $y = 0$, $y = l$, $z = 0$ and $z = l$, where l is the length that the sides would have if they were perfectly flat and mutually perpendicular. The surfaces are expected to be close to flat and orthogonal, so the error introduced by not adjusting the boundary conditions is negligible. Each surface is divided into a specified number of discrete elements that are bounded by equally spaced planes parallel to the *x*-*y*, *y*-*z*, and *x*-*z* planes (Fig. 8). For perfectly flat surfaces, these discrete elements would be squares. For non-flat surfaces, the discrete elements have non-uniform surface area and shape. The number of discrete elements should be large enough such that each element can be assumed to be essentially flat.

Fig. 9 depicts the analysis of an element of the CCR. The CCR is illuminated along the direction $-\hat{\boldsymbol{n}}_i$ by a uniform plane wave having an irradiance I_i. For each discrete element m, a ray trace is performed to determine the direction of the ray leaving the CCR. The ray starts from a reference plane where all of the rays that strike the CCR are in phase. This reference plane is required to be normal to the incident light and to pass through an arbitrary point near the CCR. The axes of the plane are chosen to be an arbitrary pair of unit vectors normal to the incident vector and each other. It is important to specify the axes for future calculations requiring change of basis. The ray first strikes the specified discrete element.

The normal vector of the discrete element is determined by computing the Jacobian of the equation describing the surface, evaluated at the center of the element. The direction of the reflected ray can be determined from the incident vector and the normal vector.

The next surface that the ray strikes, if any, is then determined, and the ray trace continues. Finally, the ray leaves the CCR and is terminated on a second reference plane, uv_m-plane. This plane is required to be normal to the ray leaving the CCR and to pass through an arbitrary point near the CCR. Unlike the first reference plane, this second reference plane is unique to each discrete element unless the surfaces are perfectly flat. The axes of this reference plane can be arbitrarily chosen to be any two unit vectors, *u* and *v*, normal to the ray from the CCR and each other. It is necessary to specify these axes to perform the required change of basis to calculate the Fraunhofer diffraction integral.

It is also important to keep track of the distance each ray propagates through the ray trace *d* and the number of reflections that occur N_{ref}. These values will be needed to specify the phase change and the transverse extent of the wave reflected from the discrete element.

The wave propagating along the path of the ray trace is a plane wave, and is nonzero only within a region given by the projection of the discrete element onto the first reference plane. When the CCR is broken into a sufficiently large number of discrete elements, the shape of this region can be approximated as a parallelogram. The boundaries of the parallelogram are determined by projecting two adjacent sides of the discrete element onto the first reference plane. Once the boundaries of the parallelogram are defined, the image can be projected to the second reference plane either inverted, for an even number of reflections, or not inverted, for an odd number of reflections. Fig. 10 shows the projected parallelogram for a particular discrete element in a CCR with four discrete elements on each surface.

It is important to note that the entire parallelogram propagates to the location of the termination on the second reference plane. The number of discrete elements must be large enough such that this method is valid. For example, if a surface has only one discrete element, the entire surface is expected to propagate to the location on a single ray trace. For certain incidence vectors, this may mean the entire surface appears to be reflected back to the source when, in actuality, only a fraction of the surface is part of the effective area.

In order to treat diffraction effects, we employ Fraunhofer diffraction theory, which is valid when the receiver lies in the far-field. More precisely, this requires that $R > a^2/\lambda$, where *R* is the distance from the aperture to the receiver, *a* is the largest dimension of the aperture, and λ is the wavelength of the light. The complex amplitude of the electric field at the observation point P contributed by discrete element *m* is given by:

$$E_m(\hat{\boldsymbol{n}}_i, \hat{\boldsymbol{n}}_o, R) = \frac{\sqrt{2I_i}e^{-i[k(R+d)+\pi N_{ref}]}}{\lambda R}\int\int_{\text{parallelogram}_m} e^{ik(Uu+Vv)/R}dS \quad , \tag{5}$$

where $k = 2\pi/\lambda$. This is illustrated in Fig. 11.

Making the substitutions $u = a_1u + b_1v$ and $v = a_2u + b_2v$, results in this expression for the electric field. (a_1, b_1) and (a_2, b_2) are vectors defined by two adjacent edges of the parallelogram as shown in Fig. 11.

$$E_m(\hat{\boldsymbol{n}}_i, \hat{\boldsymbol{n}}_o, R) = \frac{\sqrt{2I_i}e^{-i[k(R+d)+\pi N_{ref}]}}{\lambda R}(a_1b_2 - a_2b_1)\frac{\sin\alpha}{\alpha}\frac{\sin\beta}{\beta} \tag{6}$$

where $\alpha = k(b_1U + b_2V)/(2R)$ and $\beta = k(a_1U + a_2V)/(2R)$.

The sum over all discrete elements gives the complex amplitude of the total electric field at the receiver:[1]

$$E_o(\hat{\boldsymbol{n}}_i, \hat{\boldsymbol{n}}_o, R) = \sum_m E_m(\hat{\boldsymbol{n}}_i, \hat{\boldsymbol{n}}_o, R). \tag{7}$$

The irradiance at the receiver can be calculated from this total electric field using:

$$I_o(\hat{\boldsymbol{n}}_i, \hat{\boldsymbol{n}}_o, R) = \frac{1}{2}\left|E_o(\hat{\boldsymbol{n}}_i, \hat{\boldsymbol{n}}_o, R)\right|^2. \tag{8}$$

The differential scattering cross section $d\sigma(\hat{\boldsymbol{n}}_i, \hat{\boldsymbol{n}}_o)/d\Omega_o$ (m^2/sr) can be calculated from the irradiance using:

$$\frac{d\sigma(\hat{\boldsymbol{n}}_i, \hat{\boldsymbol{n}}_o)}{d\Omega_o} = \frac{I_oR^2}{I_i} \quad . \tag{9}$$

The integral of the differential scattering cross section over all observation angles equals the total scattering cross section of the CCR, $\sigma(\hat{\boldsymbol{n}}_i)$, which has units of m^2:

$$\int_{4\pi} \frac{d\sigma(\hat{\boldsymbol{n}}_i, \hat{\boldsymbol{n}}_o)}{d\Omega_o}d\Omega_o = \sigma(\hat{\boldsymbol{n}}_i) \tag{10}$$

This modeling will allow us to establish fabrication tolerances for the devices and identify design changes that will improve performance. Accurate modeling is also required to accurate predict link performance. A MATLAB simulation was written to implement this analysis. Fig. 12 is the coordinate system used to describe

1. The real, time-dependent electric field is related to the complex amplitude via $E_o(\hat{\boldsymbol{n}}_i, \hat{\boldsymbol{n}}_o, R;t) = \text{Re}[E_o(\hat{\boldsymbol{n}}_i, \hat{\boldsymbol{n}}_o, R)e^{i\omega t}]$, where $\omega = 2\pi c/\lambda$.

incident and observation directions in the simulations. The results presented in the following sections are based on this notation.

B. Performance of Ideal CCRs

Examining the relationship between the PDSCS and $-\hat{\boldsymbol{n}}_i$ will reveal the directions over which a CCR signal will transmit with sufficient power to be detected. The PDSCS for an ideal CCR can be found with the following expression.

$$\frac{d\sigma(\hat{\boldsymbol{n}}_i, \hat{\boldsymbol{n}}_i)}{d\Omega_o} = \frac{\sigma(\hat{\boldsymbol{n}}_i)^2}{\lambda^2} \tag{11}$$

This expression can be derived from (6)-(9) noting that for $\hat{\boldsymbol{n}}_o = \hat{\boldsymbol{n}}_i$, $\alpha = 0$ and $\beta = 0$, and that for each element m, $\sigma_m(\hat{\boldsymbol{n}}_i) = (a_1 b_2 - a_2 b_1)$. The PDSCS is proportional to the square of the scattering cross section.

Fig. 13 shows how the PDSCS of an ideal CCR falls off as the incident direction moves away from the cube body diagonal. Using this data, information relevant to a communication link can be found. Consider the case where a CCR is distributed with a random orientation. In other words, the interrogation direction is uniformly distributed over the entire unit sphere. The complementary cumulative distribution function, CCDF, of the PDSC normalized to the PDSCS for $-\hat{\boldsymbol{n}}_i$ along the body diagonal can be generated and is shown in Fig. 14.

Consider a communication system that requires the received power to be at least 10% of the power received interrogating along the body diagonal. In this case, Fig. 14 shows that the likelihood of being able to communicate with a randomly distributed CCR is almost 5%. If the CCR can be guaranteed to land upright, the likelihood doubles to 10%. This is because one half of the possible incident directions, all of which having $d\sigma(\hat{\boldsymbol{n}}_i, \hat{\boldsymbol{n}}_i)/d\Omega_o = 0$, are no longer being considered. The CCDF also scales with the number of CCRs assuming no two CCRs can be heard from the same interrogation direction. Therefore, if 4 CCRs were guaranteed to land upright, the likelihood of being able to communicate with one of the CCRs increases to $4 \times 10\,\%$ or 40%. Changing the size of the CCR does not affect the CCDF since the PDSCSs are normalized to the PDSCS along the body diagonal.

C. PDSCS vs. incident direction, curvature, and size for non-ideal CCRs

Now consider the case where the CCRs are non-ideal. The mirrors are defined as surfaces with spherical curvature which is a good model, as shown later. In this section, they are also assumed to be perfectly aligned. The following section discusses the effects of misalignment. It is useful to know how the reflected light from a CCR is affected by the radius of curvature, the size of the CCR, and the interrogation direction.

To investigate the effects of curvature on the received power, the PDSCS was found for varying radii of curvature and different interrogation directions. Fig. 15 is a plot of the results. In these simulations, the CCR mirrors were 250 μm on a side. For CCRs this size, a radius of curvature larger than 50 cm is desirable. Once the radius of curvature falls below 20 cm the performance of the CCR dramatically degrades.

Next the effects of increasing the size of the CCR were investigated. The effects were studied for curved and ideal CCRs from different interrogation directions. Fig. 16 shows the results. It is interesting to note that for non-ideal CCRs, given a fixed radius of curvature, increasing the CCR size can actually be harmful to the performance of the communication link.

Fig. 17 shows plots of the DSCS for an ideal CCR and non-ideal CCR for different radii for different incidence directions. When the CCR is interrogated along its body diagonal the reflected light has radial symmetry. Moving the interrogation direction away from the body diagonal reduces the PDSCS and also results in increased spreading of the reflected light. Adding curvature to the mirrors further reduces the received power, and has, in this case, increased the magnitude of the secondary lobes relative to the main lobe.

D. Misalignment and Minimum Deflection Angle

Treating the DSCS from the CCR as the combined contributions of the DSCSs of the three mirrors, the pattern from a CCR that has been misaligned can be viewed as the separation of the contributions from each mirror. Essentially, the one peak in the DSCS surrounding the imaging receiver separates into two or three peaks.

Consider a CCR with one misaligned mirror in the xy-plane as shown in Fig. 18. When the mirror is rotated an angle δ clockwise about the *x*-axis, a ray with incident direction $-\hat{\boldsymbol{n}}_i$ striking that mirror will be reflected with direction

$$\hat{\boldsymbol{n}}_r(\delta) = \boldsymbol{T}(\delta) \times -\hat{\boldsymbol{n}}_i \tag{12}$$

where

$$\boldsymbol{T}(\delta) = \begin{bmatrix} 1 & 0 & 0 \\ 0 & 1-2(\sin\delta)^2 & -\sin(2\delta) \\ 0 & -\sin(2\delta) & 1-2(\cos\delta)^2 \end{bmatrix} \tag{13}$$

The angular difference α between the reflected ray from the mirror with a tilt δ and the reflected ray for $\delta = 0$ can be found by

$$\alpha = \operatorname{acos}\left(\frac{\hat{\boldsymbol{n}}_r(\delta)\cdot\hat{\boldsymbol{n}}_r(0)}{\left|\hat{\boldsymbol{n}}_r(\delta)\right|\left|\hat{\boldsymbol{n}}_r(0)\right|}\right) \quad \textbf{(14)}$$

This angular offset is propagated through the CCR resulting in an outgoing ray that is α degrees offset from the outgoing ray in the case that $\delta = 0$. Even a small δ can drastically affect the reflected light pattern from the CCR. In the current design, tilting a single mirror in this way is the method used to direct light away from the receiving area of the lens, or turn the CCR off.

The minimum deflection angle required to turn the CCR off can be approximated for a given $-\hat{\boldsymbol{n}}_i$ using the analysis above. This method is only an approximation and should be verified with simulation since it is difficult to visualize how the combined reflected electric fields from each mirror will combine at the receiver. Let us consider an example of how to approximate the minimum deflection angle. Assume the CCR is interrogated from along its body diagonal and the receiver is far away and only captures the light incident along the direction of interrogation. If the main lobe from a single mirror is found to be 4.5 mrad wide then α must be at least 2.25 mrad, or half the lobe width. Then, from equations (12)-(14), the tilt should be at least $\delta = 1.5$ mrad. We used simulation to verify that this tilt value is sufficient to render the received signal extinct. Fig. 19(a) shows the transmitted signal for no tilt. The DSCS at the peak is 0.0414 m^2/sr. Fig. 19(b) shows the contribution from a single mirror with a main lobe 4.5 mrad wide. Fig. 19(c) shows the signal for a tilt of 1.5 mrad. The PDSCS is 0.0010 m^2/sr. The tilt reduced the received power by almost 98%.

Unfortunately, in the current design, the tilt of the offset mirror is fixed for the CCR regardless of the direction from which it is being interrogated. Therefore, the design must be made so that the CCR will function for a maximal range of incident directions. To do this design, the incident direction farthest from the body diagonal from which the CCR signal can be received should be considered. From this direction, the contribution from the mirror with the widest diffracted signal must be deflected away from the receiver to achieve high extinction. The method described above will provide a good approximation for the minimum tilt angle.

This analysis shows that tilting a single mirror by only 1.5 mrad can greatly reduce the received power. The sensitivity of the reflected light pattern to misalignment in the mirrors requires that the misalignment in the CCR must be eliminated if good CCRs are going to be made.

IV. Design and Fabrication of MEMS CCRs

In this section, the design factors that affect drive voltage, turn-on/turn-off characteristics, reflectance, flatness and alignment of mirrors in a MEMS CCR are presented. Also there is a discussion on the options for packaging.

A. MUMPS process

All of the CCRs tested in this study were fabricated in a process provided by MCNC which is now known as Cronos (http://mems.mcnc.org/). The process is called the Multi-User MEMS Process or MUMPS. Fig. 20 is a cross section of the MUMPS process. The nitride layer is not patternable and Poly0 is typically used as a ground plane. This leaves the Poly1 and Poly2 layers as the two structural layers in this process.

B. MUMPS CCR

Fig. 21 is a picture of a CCR that has not been assembled. This design has three gold coated mirrors. Each of these mirrors are 250 μm on a side. Two of the mirrors are folded out of the substrate to be normal to the surface. Mirror 1 must be raised first such that the wedge on mirror 1 can be inserted into the slot on mirror 2. These mirrors are accompanied by flip-locks used to hold the mirrors in place. The bottom mirror is the modulating mirror. After assembly, this mirror is in its offset or tilted position. The assembled CCR is shown in Fig. 22. To align the bottom mirror, a voltage difference is placed across the ground plane beneath the mirror and the mirror itself electrostatically pulling or actuating the mirror to the aligned position.

C. Hinges

Hinges allow the mirrors and locks to be raised out of the substrate plane. Unfortunately, the hinges fabricated in the MUMPS process allow for some undesired misalignment. Fig. 23 is a picture of a MUMPS hinge. Fig. 24 shows the layout of a hinge and the cross section of a raised hinge. The layout view shows that the hinge pin can shift ±2 μm along the direction of the pin. The cross section reveals that there is a 4.5 μm by 4.25 μm space containing the 2 μm by 3 μm pin. The pin can move freely within this space which may cause some misalignment in the mirrors of the CCR.

D. Flip Locks and Wedge in Slot

To support the mirrors in their upright positions as well as minimize the misalignment, flip locks are used. Fig. 25 shows a flip lock holding one of the mirrors. The slot in the lock is 1.5 μm wide which is just large enough to fit the Poly2 edge.

In addition to the flip locks, a polysilicon wedge on one standing mirror, mirror 1, is fit into a slot in the other standing mirror, mirror 2. The slot is 2 um wide which is the same width as the wedge. Fig. 26 shows this

joint from behind the CCR. This lock provides excellent alignment, but it makes the assembly of these devices more difficult.

E. Actuator

The goal is to design an actuator to align and misalign the bottom mirror with minimal voltage requirements and sufficient tilt. In the current design, the bottom mirror is actuated electrostatically. The design parameters that affect the pull-in voltage are the shape of the spring structure, the height the mirror is raised, and its angular tilt.

Accurately solving for the pull-in voltage for the actuator can be very complex because of the dynamics of the bending of the polysilicon structure acting as the spring. To gain an understanding of the design factors that affect the pull-in voltage, the problem is simplified here. The model used is depicted in Fig. 27. The variable δ is the angle at which the mirror is tilted, and ϕ is the integration variable. The mirror is assumed to be suspended over an infinite ground plane. Also, fringing of the electric field at the edges is ignored. The position of the mirror is only changed by changes in δ. In other words, the mirrors rotates about only one axis and does not translate in any direction.

Within these constraints the moment about δ, $M_{e\delta}$, due to a constant voltage placed on the mirror can be found. The potential function $\Phi(r, \phi)$ can be found by solving the Laplace equation in two dimensions [20]. The boundary conditions and the potential function are given by the following expressions.

$$\Phi(\phi = 0) = 0 \tag{15}$$

$$\Phi(\phi = \delta) = V \tag{16}$$

$$\Phi(r, \phi) = \frac{V\phi}{\delta} \qquad 0 \le \phi \le \delta, \quad r_1 \le r \le r_2 \tag{17}$$

The electric field $\hat{\boldsymbol{E}}$ can be found from the potential function.

$$\hat{\boldsymbol{E}} = -\nabla\Phi(r, \phi) \tag{18}$$

$$E_r = 0 \qquad E_\delta = -\frac{1}{r}\frac{\partial\Phi}{\partial\phi} = -\frac{1}{r}\frac{V}{\delta} \tag{19}$$

The total electrostatic energy is:

$$U = \frac{\varepsilon_0}{2}\int|\hat{\boldsymbol{E}}|^2 dV \tag{20}$$

$$U = \frac{\varepsilon_0}{2}\int_0^W dy \int_{r_1}^{r_2} r\,dr \int_0^{\delta} \left(-\frac{1}{r}\right)^2 \left(\frac{V}{\delta}\right)^2 d\phi \tag{21}$$

$$U = \frac{\varepsilon_0 V^2 W}{2\delta} \ln\left(\frac{r_2}{r_1}\right) \tag{22}$$

In this expression, ε_0 is the permittivity of free space (8.8542×10^{-12} F/m).

The moment $M_{e\delta}$ can be found from the total energy.

$$M_{e\delta} = -\frac{\partial U}{\partial \delta}\bigg|_{V_{const}} = -\frac{K_e V^2}{\delta^2} \tag{23}$$

where

$$K_e = \frac{\varepsilon_0 W}{2} \ln\left(\frac{r_2}{r_1}\right) \tag{24}$$

The opposing moment due to the spring, $M_{s\delta}$, is a function of the shape and dimensions of the polysilicon support. The polysilicon beams can bend due to a moment or force or experience torsional deformation due to a moment [19]. Fig. 28 shows the bending of a beam due to a force and moment. The deflection $y(x)$ due to the force F and moment M_0 is given by:

$$y(x) = \frac{1}{EI}\left[\frac{Fx^2}{6}(3L - x) + \frac{M_0 x^2}{2}\right] \tag{25}$$

The angular deflection is:

$$\theta(x) = \frac{1}{EI}\left[Fx\left(L - \frac{x}{2}\right) + M_0 x\right] \tag{26}$$

In these equations, E is Young's modulus and I is the moment of inertia of the beam cross section which is given by:

$$I = \frac{a^3 b}{12} \tag{27}$$

where a is the height of the beam and b is the width of the beam.

Under a torsional load, M_t, the beam will deform such that the two opposite faces rotate and angle α with respect to one another (Fig. 29).

$$\alpha = \frac{M_t L}{JG} \tag{28}$$

where G is the shear modulus of the beam and J is the polar moment of inertia. G is related to E and ν, Possion's ratio by:

$$G = \frac{E}{2(1+\nu)} \tag{29}$$

For a rectangular cross section,

$$J = ca^3 b \tag{30}$$

where a and b are the dimension of the cross section ($b > a$) and c is a function of a/b. Table 1 gives some values of c.

Based on the polysilicon spring, (26) and (28) can be used to find a relation between $M_{s\delta}$ and δ.

$$M_{s\delta} = K_s(\delta_0 - \delta) \tag{31}$$

where δ_0 is the equilibrium angle with no voltage applied.

This results in a total moment $M_{tot\delta}$ given by the following expression.

$$M_{tot\delta} = M_{s\delta} + M_{e\delta} = K_s(\delta_0 - \delta) - \frac{K_e V^2}{\delta^2} \tag{32}$$

The minimum pull-in voltage is the minimum voltage V for which $M_{tot\delta} \le 0$ for all δ in the range $0 \le \delta \le \delta_0$. Solving $M_{tot\delta} \le 0$ for V gives:

$$V \ge \sqrt{\frac{K_s \delta^2 (\delta_0 - \delta)}{K_e}} \tag{33}$$

The value of δ that maximizes the right hand side of (33) is $\delta = \frac{2}{3}\delta_0$. Therefore, the minimum pull-in voltage is given by (33) with $\delta = \frac{2}{3}\delta_0$.

$$V_{min} = \sqrt{\frac{4K_s \delta_0^3}{27K_e}} \tag{34}$$

As stated earlier, this expression for the minimum pull-in voltage is not exact, but it does give the designer an idea of how changing the polysilicon spring structure and the tilt angle will affect the pull-in voltage. The design should be made to minimize δ_0 while satisfying the minimum deflection requirement. Reducing the spring constant K_s will also reduce the minimum pull-in voltage.

Unfortunately, the rigidity of the spring cannot be made arbitrarily small. Once the mirror has been pulled down to its aligned position, it is resting on the bumpers that prevent it from touching the ground plane. The mirror has a tendency to adhere to the bumpers after being pulled down. The spring must be made rigid enough to overcome this sticking.

The bumpers are there to prevent the mirror from contacting the ground plane. This would cause a short and burn out the device. They should be made small to minimize the surface area in contact with the mirror. This will help to reduce the sticking. Fig. 30 illustrates the bumpers used in our design.

The resonant frequency, ω_0, of the actuator gives an upper bound to the maximum operating frequency of the device. Ignoring the effects of damping, the resonant frequency is given by:

$$\omega_0 = \sqrt{\frac{K_s}{I_m}} \tag{35}$$

where I_m is the mass moment of inertia of the mirror about the axis of rotation.

$$I_m = \frac{1}{3}\rho_l(r_2^3 - r_1^3) \tag{36}$$

where ρ_l is the linear mass density of the mirror (total mass of the mirror divided by the length). Squeeze-film damping does play a large role in the dynamics of the actuator, but this effect is difficult to characterize and will not be considered in this paper. When it is considered, the device's resonant frequency will be lower than that given by (34).

F. Mirrors

MCNC mirrors are subject to some curvature due to the fabrication process. This is caused by the difference in thermal expansion coefficients between gold and polysilicon. In studies conducted by Patrick Chu, the flattest metal-coated mirrors were fabricated by sandwiching Ox2 between Poly1 and Poly2 (Fig. 31)[14]. The metal layer is necessary to increase the reflectance of the mirrors.

The curvature in the mirrors should be reduced as much as possible to improve the optical performance of the CCRs. One way to reduce the mirror curvature is to change the thicknesses of the layers in the mirror.

Another may be to deposit a metal layer other than gold onto the mirrors, which may also improve the reflectance.

It is of interest to understand how the layer thicknesses affect the curvature of the mirrors, and to know what other material properties affect the curvature. An expression for the radius of curvature for a bimetallic circular plate is presented below. The circular plate is considered rather than a rectangular plate because the analysis is simpler and serves as a good approximation of the effect varying layer thicknesses and material properties will have on the curvature.

The curvature of a circular plate under a uniform temperature difference between the top and bottom surface can be predicted as described in [15]. This solution is based on the following assumptions.

1) Plate is flat, has uniform thickness, and is composed of a homogeneous isotropic material.

2) The thickness of the plate is not more than about 1/4 of the least transverse dimension and the maximum deflection is not more than about 1/2 the thickness.

3) All forces are normal to the plane of the plate.

4) the plate is nowhere stressed beyond the elastic limit.

For a uniform temperature difference ΔT between the bottom and top surface from r_0 to a (Fig. 32), the deflection y is given by

$$y = K_y \frac{\gamma \Delta T a^2}{t} \tag{37}$$

where $K_y = -\frac{1}{2}$ for $\frac{r_0}{a} = 0$ which is the case being considered. γ is the coefficient of thermal expansion.

The same equation can be used to solve for the deflection of a bimetallic plate (Fig. 33) subjected to a change in temperature change away from the temperature at which the plate is flat T_0 with the following substitution:

$$\frac{\gamma \Delta T}{t} = \frac{6(\gamma_b - \gamma_a)(T - T_0)(t_a + t_b)}{t_b^2 K_{1p}} \tag{38}$$

where

$$K_{1p} = 4 + 6\frac{t_a}{t_b} + 4\left(\frac{t_a}{t_b}\right)^2 + \frac{E_a t_a^3 (1 - \nu_a)}{E_b t_b^3 (1 - \nu_b)} + \frac{E_b t_b (1 - \nu_a)}{E_a t_a (1 - \nu_b)} \tag{39}$$

ν is Poisson's ratio and E is Young's modulus of elasticity.

A bimetallic plate deforms laterally into a spherical surface when its uniform temperature differs from T_0 [15]. The radius of curvature can be approximated by the following expression.

$$\rho \approx \frac{a^2}{2y} \tag{40}$$

After substitutions, the final expression for the radius of curvature is

$$\rho = \frac{t_b^2 K_{1p}}{6(\gamma_b - \gamma_a)(T - T_0)(t_a + t_b)} \tag{41}$$

The mirrors that have been fabricated in the MUMPS process actually have four layers, but the theory is useful in searching for a means to fabricate flatter mirrors. If the poly-oxide-poly portion is treated as one layer and the gold another, then the effects of varying the thickness of the gold layer can be predicted.

Alternative metals should also be considered. Some alternatives such as silver, aluminum, or a dielectric have higher reflectance. Silver has excellent reflectance at all wavelengths greater than about 380 nm. However, silver can be excluded because of its tendency to tarnish. Also, the dielectric mirror would be very difficult to attach onto a MEMS structure at this time. Aluminum is an attractive alternative depending on the wavelength of light used to interrogate the CCR. It has a higher reflectance than gold for wavelength less than 600 nm. However, the coefficient of thermal expansion of aluminum is higher than that of gold.

Calculations were performed to observe the effects of varying layer thicknesses and metal properties. The bottom layer, metal b. was assumed to be polysilicon, and metal a was either gold or aluminum. Values for Young's modulus for polysilicon, gold, and aluminum have been reported as 169 GPa, 80 GPa, and 69 GPa, respectively [10][11]. Also, Poisson's ratio for polysilicon was reported as being 0.22. The coefficients of thermal expansion of gold and aluminum are 14.3×10^{-6} /℃ and 23×10^{-6} /℃. Unfortunately, values for the coefficient of thermal expansion of polysilicon and Poisson's ratio for gold and aluminum have not been reported. For simulation purposes, the coefficient of thermal expansion for metal b was set at 10×10^{-6} /℃ which is simply a value less than that of gold. Poisson's ratio for gold and aluminum layer was assumed to be the same as polysilicon. The exact temperature difference is also unknown so $(T - T_0)$ was assumed to be 100 ℃.

Fig. 34 shows the results for varying thickness of metal a. The thickness of metal b was fixed at 3 μm. This plot shows that decreasing the thickness of the metal a layer will increase the radius of curvature. Increasing the thickness of metal a, past a certain point will also begin to increase the radius of curvature, but the rate of increase is much slower and the thickness required to achieve the required mirror flatness would be

too large. This plot also shows that the gold metal has a higher radius of curvature than the aluminum metal. This is mostly due to the larger coefficient of thermal expansion for aluminum.

Fig. 35 shows the effects of varying the thickness of metal b. The thickness of metal a was fixed at 0.5 μm Increasing the thickness of metal b increases the radius of curvature. However, the rate of increase is much slower than that for reducing the thickness of metal a.

The thickness of metal a should be minimized to maximize the radius of curvature. However, the thickness of the metal must be several times larger than the skin depth d_{skin} of the metal such that the metal is reflective. The skin depth for a nonmagnetic metal can be calculated with the following expression:

$$d_{skin} = \frac{1}{\sqrt{\pi f \mu_0 \sigma}} \tag{42}$$

In this expression, f is the frequency of the light, μ_0 is the permeability of free space ($4\pi \times 10^{-7}$ N/A^2), and σ is the metal's conductivity. The conductivities of gold and aluminum are 4.1×10^7 S/m and 3.5×10^7 S/m, respectively. The skin depth of aluminum is therefore slightly less than that of gold.

G. Packaging

MEMS CCRs are fragile and can be damaged by the surrounding environment so packaging is necessary to protect the devices. The packaging must be transparent and have low reflectivity so that it does not reduce the power of the interrogating and reflected light. There are several options for the shape of the packaging. A hemispherical shape, a raised flat plate, and square pyramid shape are considered (Fig. 36).

The hemispherical shape is attractive because commercial vendors can be found to provide them. Also, multiple CCRs can be placed within the same package. The trouble with this shape is that there will be lensing effects if the diameter of the hemisphere is too small. This can affect the performance of the CCR.

A flat plate supported over the device(s) will not have the lensing effects of the hemisphere. However, the package must allow light to pass for all useful incident directions. To avoid light being blocked by the edge of the package, the plate must be made relatively large. Also, the reflectivity of the plate increases as the direction of incidence approaches glancing incidence. This is an easy packaging option to use and multiple CCRs can be placed under the same plate.

A square pyramid shape whose surfaces are normal to the body diagonals of the CCRs is an attractive option. The useful incident directions will be closer to being normal to the packaging surface than for the flat plate, reducing the loss due to reflection. This package can only contain up to four CCRs. It may also be more difficult to fabricate this package that the other two types.

V. Experimental Characterization of MEMs CCRs

A. Optical Characteristics

Using an interferometer constructed by Matt Hart at U.C. Berkeley [18], mirror surface data and misalignment data was acquired for several CCRs. The mirrors fabricated in the MCNC process have spherical curvature as the theory predicts. Fig. 37 is a plot of a typical set of surface data along a line bisecting a mirror. The results show that the radius of curvature was approximately 15 mm. These mirrors are from MCNC run #28. Typical mirrors from MUMPS run #30 had radii of curvature around 10 mm. Patrick Chu reported a radius of curvature of 21.5 mm for the same mirror layout, but a different MUMPS run [14]. The curvature is likely to vary from run to run. Regardless or this inconsistency, the radius of curvature is at least an order of magnitude too small for these to be considered good CCRs.

The surface data for each mirror of a CCR was acquired by first aligning one mirror surface to the interferometer and then turning the CCR exactly 90° for each of the other two mirror measurements. Using this method, the misalignment between each of the mirrors could be recovered. Table 2 presents the results for several CCRs based on the notation in Fig. 38. Δ is the deviation from 90° or 1.5708 rad.

The only consistency in the data are the signs of the deviations. The angle α is consistently less than 90° and β and γ are greater than 90°. The least amount of deviation was in β which is probably due to the wedge fitting in to the slot. Clearly, the misalignment in the current CCR design is too large and too inconsistent. This issue must be addressed in further CCR designs.

B. Electrical and Mechanical Characteristics

The design for the tilted bottom mirror was originally created by Patrick Chu [12]. The process for tilting the bottom mirror is depicted in Fig. 39. First, the jack is pushed to raise the support plate. Then, the sliding plate is slid beneath the support beam. Finally, the jack is released so that the support plate is resting on the sliding plate. Fig. 40 shows a cross section of this design. For mirrors that are 250 μm on a side, the tilt is approximately 45 mrad and the distance from the ground plane to the end of the offset mirror is approximately 14-16 μm depending on the design of the spring or support beams.

A large variety of different spring designs were fabricated and tested. Some of the designs tested are depicted in Fig. 41. Many of the spring designs were fabricated in the Poly1 layer as well as the Poly2 layer. The dimensions of each spring were also varied as well as the spacing between the mirror and the support plate. The design requiring the lowest drive voltage while consistently returning the mirror to its tilted position was found to be a single beam structure fabricated in Poly2. The design is shown in Fig. 42 and is also shown in the SEM in Fig. 39. Typical values for the drive voltage for this design range from 7 to 11 V.

Using the analysis in Section IV.E and considering only the torsional bending of beam 1 and the bending of beam 2, the following is the expression for the spring contant.

$$K_s = \left(\frac{L_1}{J_1 G} + \frac{L_2}{E I_2} \right)^{-1} \quad \textbf{(43)}$$

Table 3 lists all the values used to calculate the pull-in voltage. The end result is $V \geq 4.88$ V. The theoretical pull-in voltage is less than the measured pull-in voltages, but as mentioned earlier, the analysis provides a means to improve the design and not necessarily accurately predict the pull-in voltage.

The turn-on and turn-off characteristics of this design were measured. Fig. 43 shows plots of the received signal due to a step input drive voltage from low-to-high and high-to-low. The rise time is approximately 2 ms and the fall time is approximately 6.5 ms. Notice that there is a second peak in the high-to-low transition. This may be due to the mechanical ringing of the mirror after the electrostatic force is removed and the flexed beam snaps it up to the tilted position. This results in a maximum operating frequency for full voltage swing of about 118 Hz. In other words, the CCR can be driven by a square wave with frequency up to 118 Hz.

The calculated resonant freqency is about 6.8 kHz which is orders of magnitude larger than the measured maximum operating frequency. If the second peak in the high-to-low transition was in fact due to the ringing of the mirror, it would suggests a resonant frequency of about 200 Hz. Clearly, the effects of squeeze-film damping greatly affect the transitions in the actuator.

VI. Discussion

A. Agreement between Modeling and Experiment

The corner cubes that were fabricated in the MCNC were too non-ideal to allow us to compare their optical properties (e.g. DSCS) to the theoretical results of Section III. The mirrors were too curved and the misalign-ment was too great. However, the CCRs were still able to communicate. A system similar to the one shown in Fig. 6 with the imaging receiver replaced by a bare die was constructed to capture the reflected light pattern. Fig. 44 shows the received light from the CCR in the on and off states. The image captured by the die for the CCR in its on state is only a small fraction of the far-field pattern of the light reflected by the CCR. If the CCRs were good, this pattern would resemble the patterns seen in Fig. 17.

The bare die used to capture the image was replaced by a video camera, and the images that were captured for the CCR in its on and off states are shown in Fig. 45. There is a clear difference between the on and off

states that can be detected by an imaging receiver. The fact that the CCRs work at all with such a high degree of misalignment and curvature may be that one error is compensating for the other. If the mirrors were flat and the misalignment was as the data reflects, the CCRs would not be able to direct light to the receiver. The curvature is the mirror is helping to compensate for the misalignment so at least part of the light can be directed to the receiver.

B. Optimization of MEMS CCRs:

The three most important issues to resolve are reducing the mirror curvature, improving the alignment between the mirrors, and optimizing the design of the actuator for low drive voltage and high operating frequency.

1. Within MUMPS process

There are a number of techniques to improve the CCR design while continuing to use the MUMPS process. To reduce the mirror curvature, the mirrors can be fabricated without any metal coating. The metal layer can be deposited separately after the devices have already be released giving the designer control over the type of metal and the thickness of the metal that is applied. This will allow the designer to minimize curvature and maximize reflectance. By properly protecting the electrical contacts, a mask for the metal layer may not even be necessary. The metal can simply be deposited over the entire device. The type of metal should be determined by the wavelength at which the system will operate. The metal layer should be made as thin as possible to minimize curvature. However, the metal layer must be several times thicker than the skin depth of the metal used. For example, if the system was using red light with a wavelength of 632 nm the skin depth of aluminum is 3.9 nm and is greater than the skin depth of gold which is 3.6 nm. At this wavelength, the reflectance of gold is also slightly greater than aluminum. In addition, the curvature of gold for the same thickness is less than that of aluminum. At this wavelength, gold is a better material to use than aluminum. However, if the system were to use green light with a wavelength of 543 nm, the choice is less obvious. The skin depth of aluminum at this wavelength is 3.6 nm, and the skin depth of gold is 3.3 nm. The reflectance of of gold is about 0.5, and the reflectance of aluminum is about 0.9. This difference is reflectance results in 5.8 times greater power for aluminum than gold. Unfortunately, the curvature of the minimum thickness aluminum mirror with be greater than the curvature of a minimum thickness gold mirror and could cause a greater loss than the gain from the reflectance. This loss cannot be predicted at this time since values needed to predict the curvature are still unknown.

The alignment can be improved by using multiple hinges at both ends of the mirror. This will reduce the amount that the pin can swivel. More specifically, Mirror 1 (Fig. 21) should have another hinge on the end that

only has one hinge currently. Also, the Poly2 extension from Mirror 1 should be shortened so that the flip lock is closer to the mirror. There are certainly more ways to improve on the alignment without restricting oneself to the current design, and the data suggests that this will be necessary once the mirrors are made flatter.

The tilt on the current actuator is larger than it needs to be for communication purposes. One way to reduce the tilt is to remove the Poly1 layer from the support plate. This should reduce the tilt from about 45 mrad to approximately 23 mrad. Once the tilt is reduced, the support beam(s) will need to be redesigned and could be made more rigid to improve the operating frequency. There are many ways to tilt a mirror or mirrors of the CCR, and alternative designs may prove to perform better.

2. Best process to use for CCRs

The MCNC MUMPS process can be used to make working CCRs, but it may not be possible to make ideal or near-ideal CCRs. In addition, the process of assembling the MUMPS devices is difficult and results in a lower yield than is desirable. Currently, CCRs are also being developed in different MEMS processes such as LIGA which is a process that allow the CCRs to be fabricated with the mirrors already properly aligned. In addition, the mirrors can be made very thick to minimize curvature. There are problems with the this process as well. The drive voltage is probably going to be much higher, and the size of the entire structure with be larger.

CCRs are also being made in the SANDIA process which is currently a three-structural poly layer process and is likely to increase the number of structural layers in the future. Increased structural layers gives more freedom in the design and can lead to easy-to-assemble CCRs with similar or better performance than the MUMPS CCRs.

It is difficult to define a process to make ideal CCRs. The process must have thicker or more rigid structural layers than MUMPS so that the curvature in the mirrors is minimized. It should also provide enough flexibility such that a well-aligned CCR that is easy to assemble can be designed. The process must also allow for the design of an actuator with a low drive voltage and high operating frequency.

VII. Conclusions

Micromachined corner cube retroreflectors that can be used to transmit data in a free-space optical communication system have been fabricated and tested. The results show that a communication link employing these devices can be created, but the performance is far from the theoretical limit. An analysis to determine the DSCS of CCRs has also been presented, and can be used to predict the performance of CCRs and determine device tolerances. There are a number of ways to improve the performance of CCRs. The mirrors can be made

more flat, the alignment can be improved, the drive voltage can be reduced, and the operating frequency can be increased.

VIII. References

[1] M. Born and E. Wolf, *Principles of Optics*, Sixth Edition, Pergamon Press, 1980.

[2] J.G. Proakis, *Digital Communications*, Third Edition, Mc-Graw Hill, 1995.

[3] J.B. Carruthers and J.M. Kahn, "Angle Diversity for Nondirected Wireless Infrared Communication", subm. to *IEEE Trans. on Commun.*, July 1997.

[4] J.M. Kahn and J.R. Barry, "Wireless Infrared Communications", *Proc. of the IEEE*, pp. 265-298, February 1997 (Invited Paper).

[5] IEC825-1 "Radiation Safety of Laser Products' Equipment Classification, Requirements, and User's Guide" (1993).

[6] A.S. Tanenbaum, *Communication Networks*, Third Edition, Prentice-Hall, 1996.

[7] F. Gfeller, W. Hirt, M. de Lange and B. Weiss, "Wireless Infrared Transmission: How to Reach All Office Space", *Proc. of IEEE Vehicular Technol. Conf.*, pp. 1535-1539, Atlanta, Georgia, April, 1996.

[8] E. Hecht, *Optics*, Second Edition, Addison-Wesley, 1990.

[9] V. S. Hsu, J. M. Kahn, and K. S. J. Pister. "Wireless communications for smart dust" Technical Report UCB/ERL M98/2, UC Berkeley Electronics Research Laboratory, Berkeley, CA 94720, December 1998.

[10] W. N. Sharpe, B. Yuan, R. Vaidyanathan, and R. L. Edwards. "Measurements of Young's Modulus, Poisson's ratio, and tensile strength of polysilicon", *Proc. of IEEE Micro Electro Mechanical Systems Workshop*, Nagoya, Japan, 1997.

[11] B. Rashidian and M.G. Allen. "Electrothermal microactuators based on dielectric loss heating", *Proc. of IEEE Micro Electro Mechanical Systems Workshop*, pp. 24-29, Florida, February,1993.

[12] P. B. Chu, N. R. Lo, E. C. Berg, and K. S. J. Pister. "Optical communication using micro corner cube reflectors", *Proc. of IEEE Micro Electro Mechanical Systems Workshop*, pp. 350-355, Nagoya, Japan, 1997.

[13] D. S. Gunawan. Micromachined corner cube reflectors as a communication link. Master's thesis, University of California, Los Angeles, 1994.

[14] P. B. Chu. Optical communication with micromachined corner cube reflectors. PhD thesis, University of California, Los Angeles, 1998.

[15] W. C. Young, *Roark's Formulas for Stress and Strain*, Sixth Edition, McGraw-Hill, 1989.

[16] M. W. Judy, Y-H Cho, R. T. Howe, and A. P. Pisano. "Self-adjusting microstructures (SAMS)", *Proc. of IEEE Micro Electro Mechanical Systems Workshop*, pp. 51-56, Nara, Japan, Jan. 30 - Feb. 2, 1991.

[17] N. N. Rao, *Elements of Engineering Electromagnetics*, Fourth Edition, Prentice Hall, 1994.

[18] M. R. Hart, R. A. Conant, K. Y. Lau, R. S. Muller. "Time-resolved measurement of optical MEMS, using stroboscopic interferometry"; *Transducers '99*, pp. 470-473, Sendai, Japan, June 1999.

[19] K. S. J. Pister. Hinged polysilicon structures with integrated CMOS thin film transistors. PhD thesis, University of California, Berkeley, 1992.

[20] J. D. Jackson, *Classical Electrodynamics*, Second Edition, John Wiley and Sons, 1975.

IX. Tables

Table 1: Rectangular polar moment of inertia constant c.

a/b	c
1.0	0.141
1.5	0.196
2.0	0.229
5.0	0.291
10.0	0.312
∞	0.333

Table 2: Misalignment data.

CCR#	α (rad)	Δα	β	Δβ	γ	Δγ
1	1.5697	-0.0011	1.5726	0.0018	1.5758	0.0050
2	1.5671	-0.0037	1.5713	0.0006	1.5721	0.0013
3	1.5680	-0.0028	1.5728	0.0020	1.5746	0.0038

Table 3: Values used to compute pull-in voltage and resonant frequency.

Parameter	Value
a_1	1.5 μm
b_1	10 μm
J_1	1.013×10^{-23} m^4
L_1	60 μm
G	69.26 GPa
a_2	1.5 μm
b_2	10 μm
I_2	2.813×10^{-24} m^4
L_2	135 μm
E	169 GPa
r_1	83.6 μm
r_2	333.6 μm
δ_0	45 mrad
W	250 μm
ρ_l	4.835×10^{-6} kg/m

X. Figures

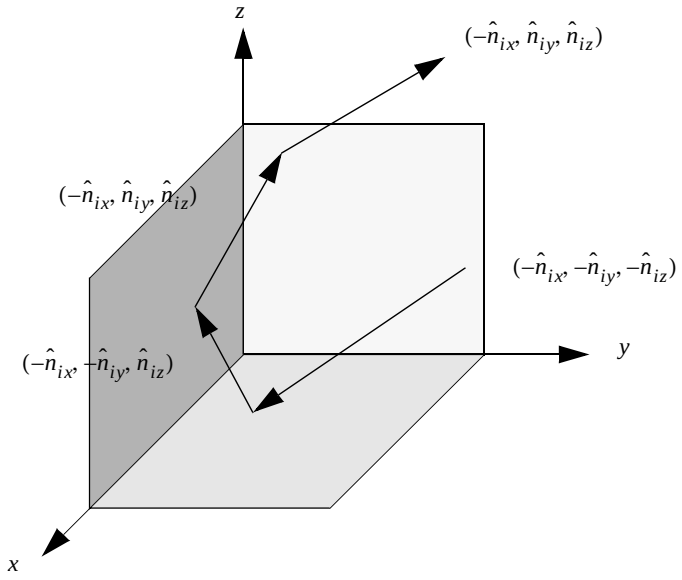

Fig. 1. Raytrace through an ideal CCR.

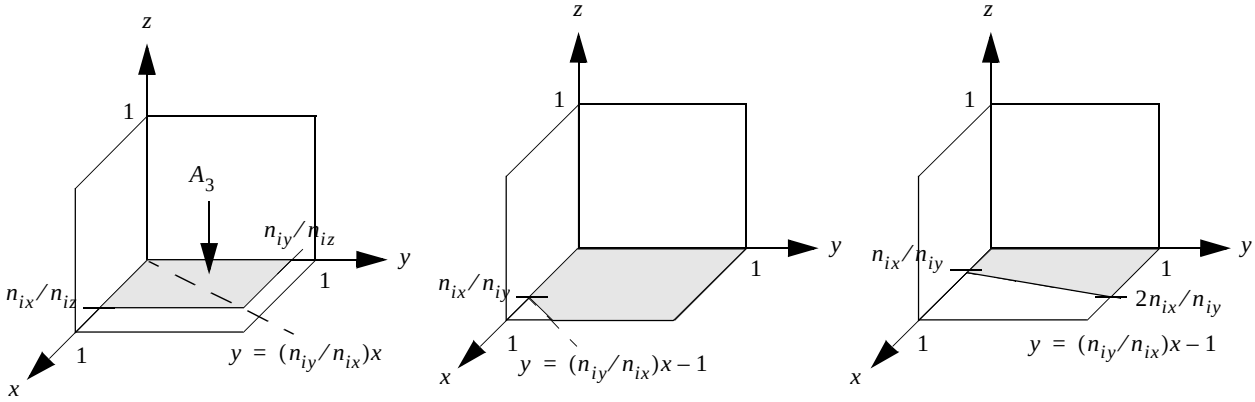

(a) $n_{iz} > n_{iy} > n_{ix}$

$$A_3 = \frac{n_{ix} n_{iy}}{n_{iz}^2}$$

(b) $2n_{ix} > n_{iy} > n_{ix} > n_{iz}$

$$A_3 = 1 - \frac{1}{2}\left(1 - \frac{n_{ix}}{n_{iy}}\right)\left(\frac{n_{iy}}{n_{ix}} - 1\right)$$

(c) $n_{iy} > 2n_{ix} > n_{iz}$ or

$n_{iy} > n_{iz} > n_{ix}, n_{iy} > 2n_{ix}$

$$A_3 = \frac{3}{2}\frac{n_{ix}}{n_{iy}}$$

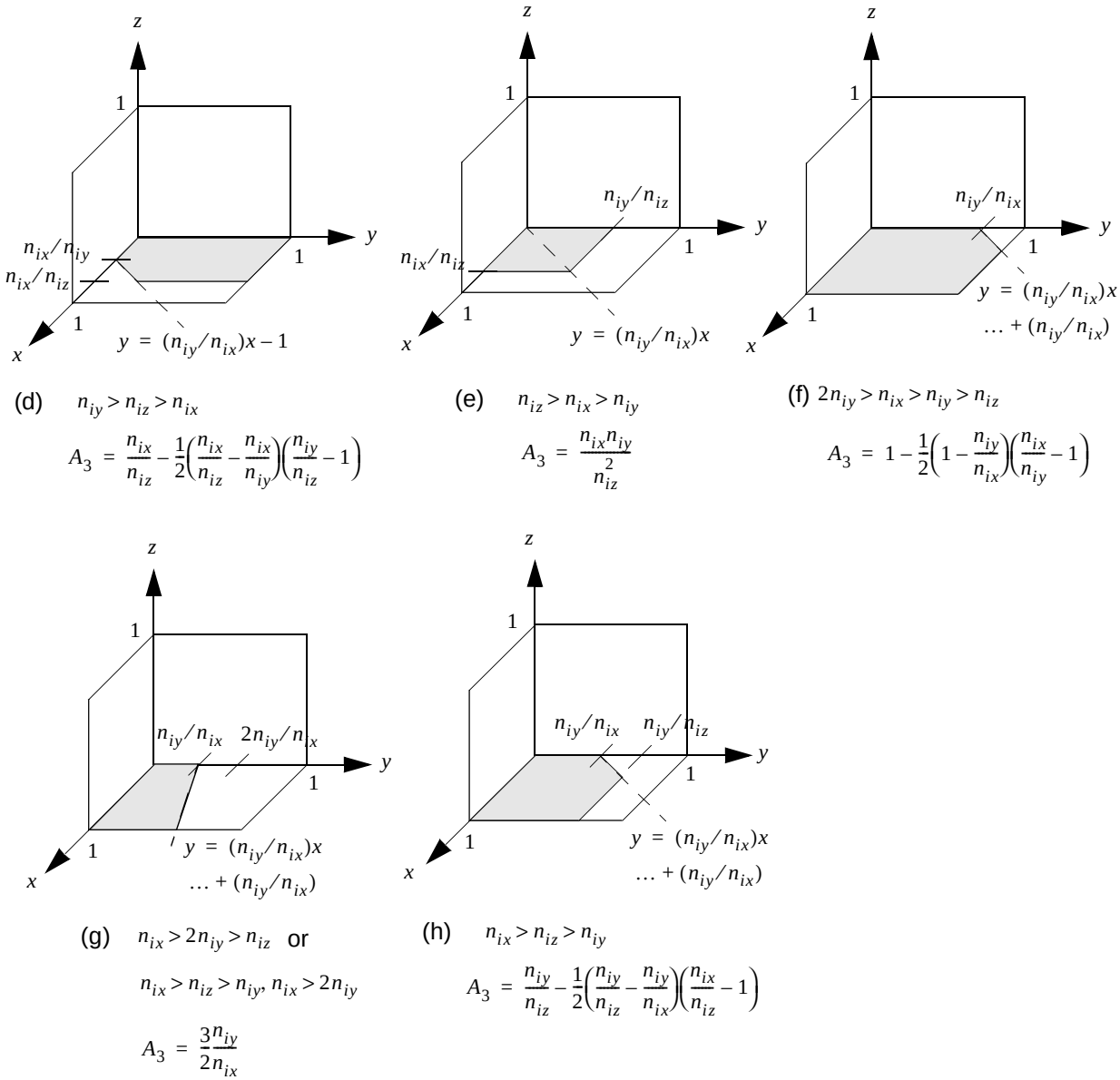

(d) $n_{iy} > n_{iz} > n_{ix}$

$$A_3 = \frac{n_{ix}}{n_{iz}} - \frac{1}{2}\left(\frac{n_{ix}}{n_{iz}} - \frac{n_{ix}}{n_{iy}}\right)\left(\frac{n_{iy}}{n_{iz}} - 1\right)$$

(e) $n_{iz} > n_{ix} > n_{iy}$

$$A_3 = \frac{n_{ix} n_{iy}}{n_{iz}^2}$$

(f) $2n_{iy} > n_{ix} > n_{iy} > n_{iz}$

$$A_3 = 1 - \frac{1}{2}\left(1 - \frac{n_{iy}}{n_{ix}}\right)\left(\frac{n_{ix}}{n_{iy}} - 1\right)$$

(g) $n_{ix} > 2n_{iy} > n_{iz}$ or

$n_{ix} > n_{iz} > n_{iy}$, $n_{ix} > 2n_{iy}$

$$A_3 = \frac{3}{2}\frac{n_{iy}}{n_{ix}}$$

(h) $n_{ix} > n_{iz} > n_{iy}$

$$A_3 = \frac{n_{iy}}{n_{iz}} - \frac{1}{2}\left(\frac{n_{iy}}{n_{iz}} - \frac{n_{iy}}{n_{ix}}\right)\left(\frac{n_{ix}}{n_{iz}} - 1\right)$$

Fig. 2. Calculating the effective area of an ideal CCR.

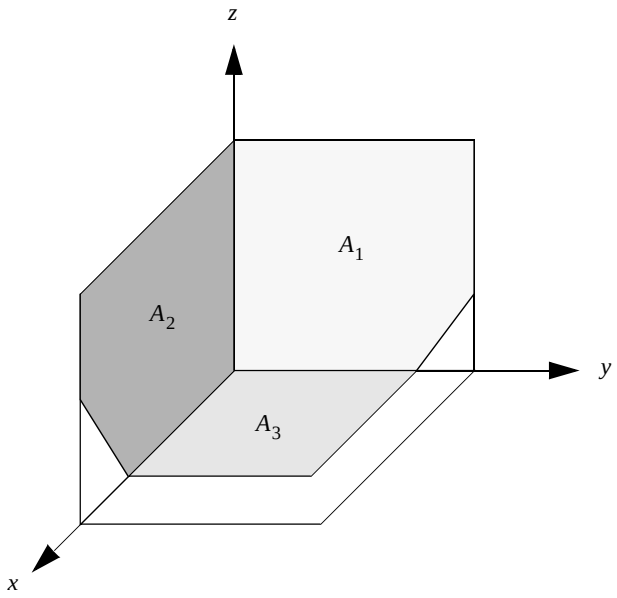

Fig. 3. Calculating scattering cross section of an ideal CCR.

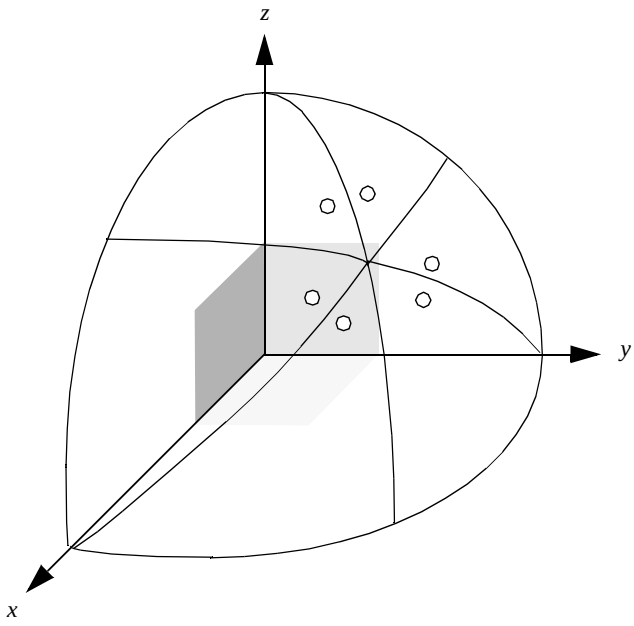

Fig. 4. Three-fold rotational symmetry of an ideal CCR.

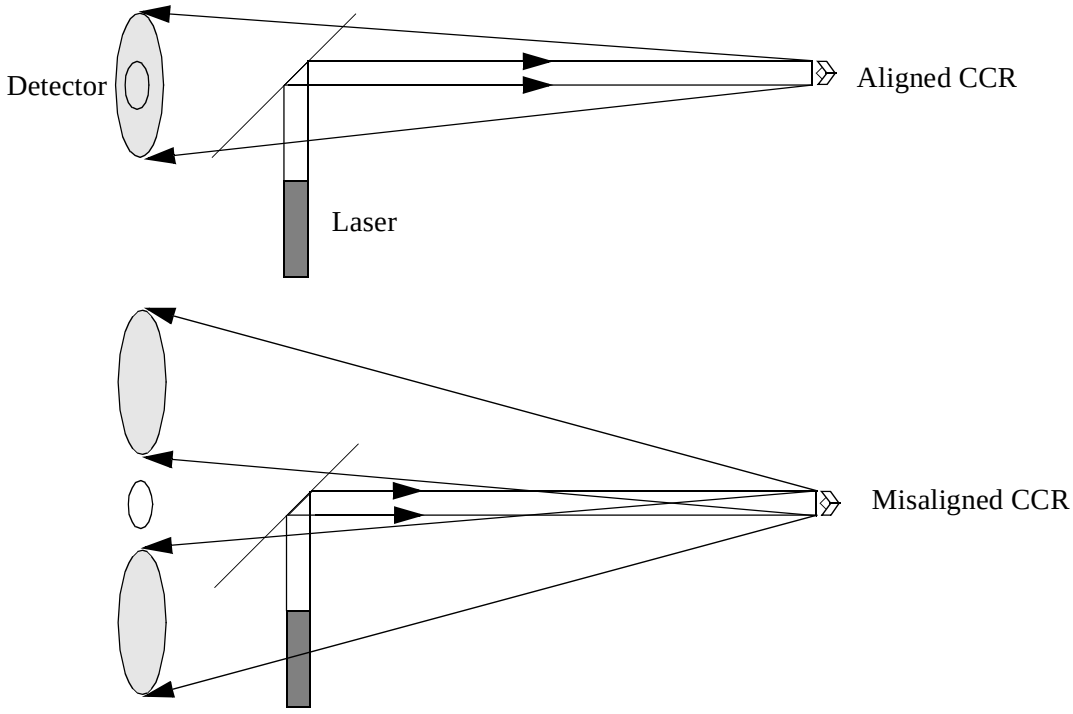

Fig. 5. Optical communication with a CCR.

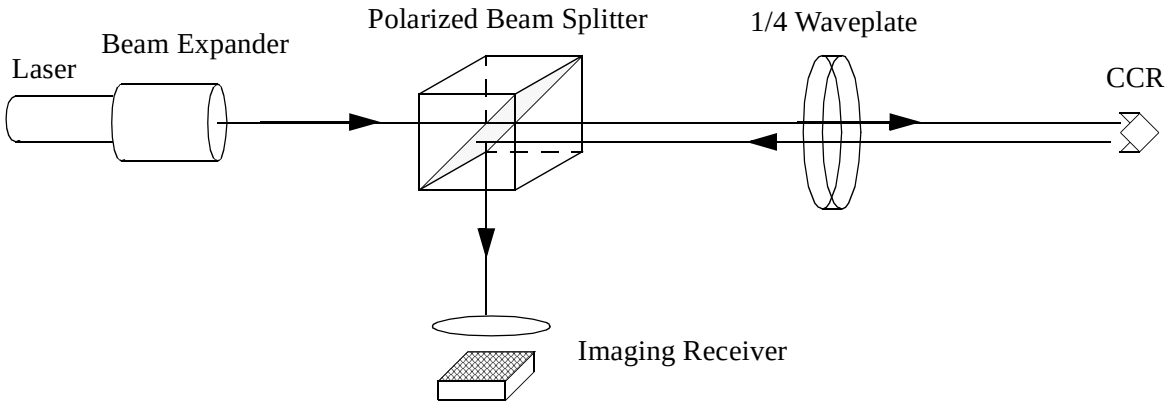

Fig. 6. System designed to separate the interrogation light and the received light.

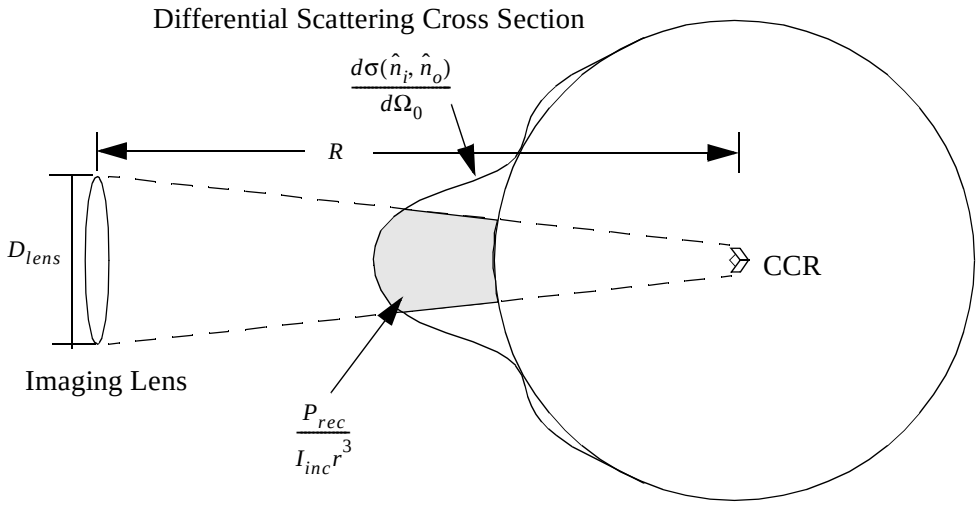

Fig. 7. Calculating the power received by an imaging receiver from a CCR.

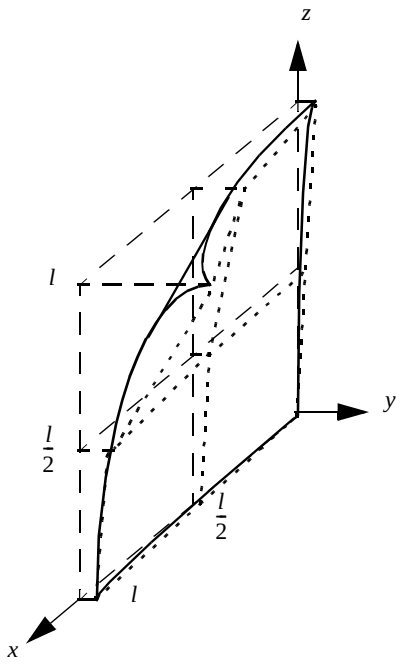

Fig. 8. Discretization of the CCR surfaces.

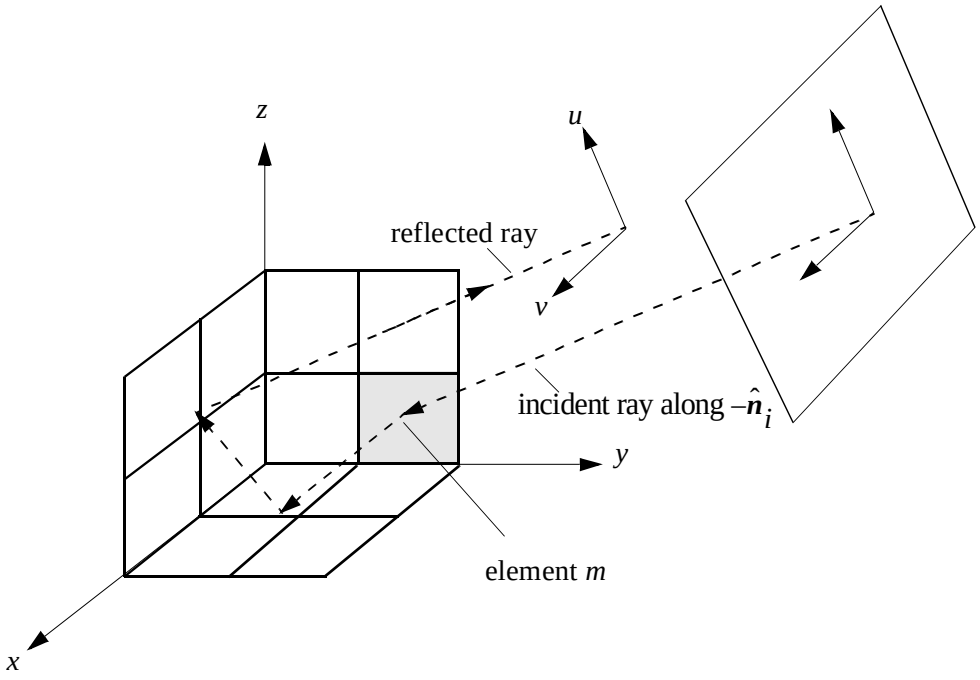

Fig. 9. Analysis of element *m* in the CCR.

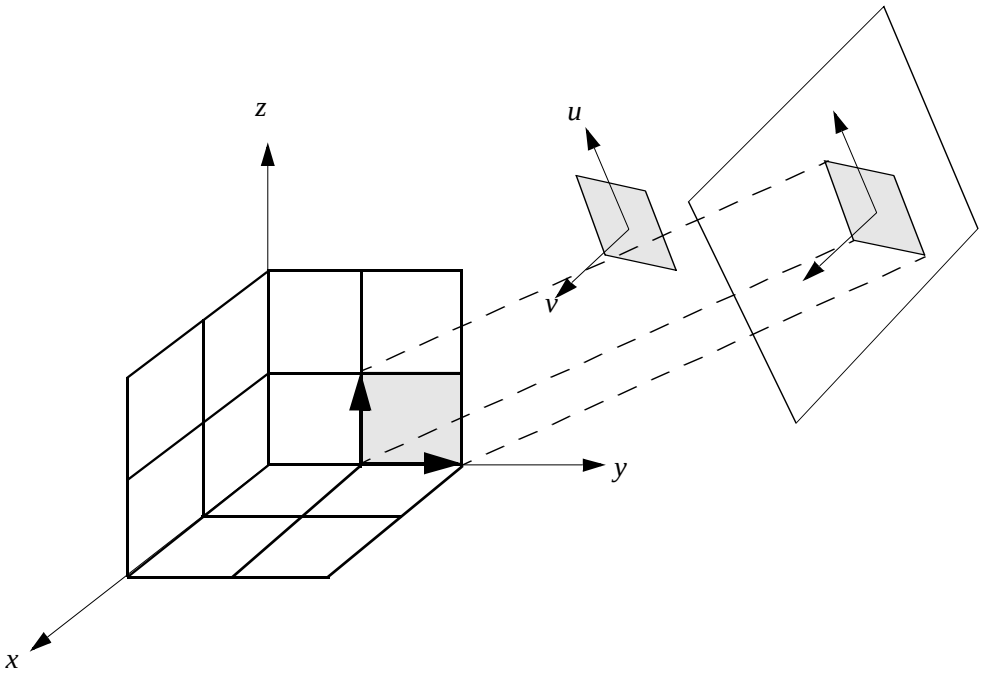

Fig. 10. Projecting the parallelogram.

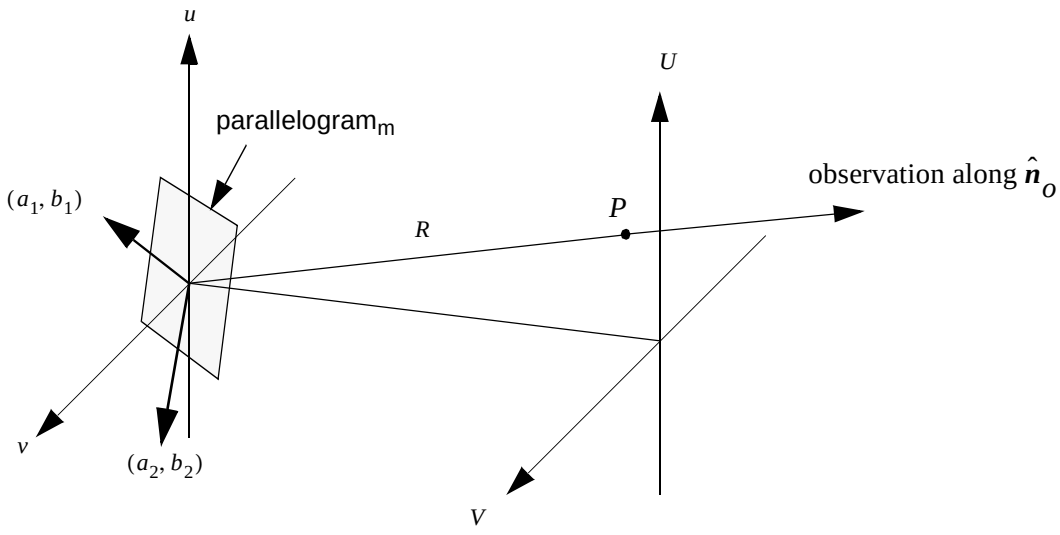

Fig. 11. Calculating the Fraunhoffer diffraction integral.

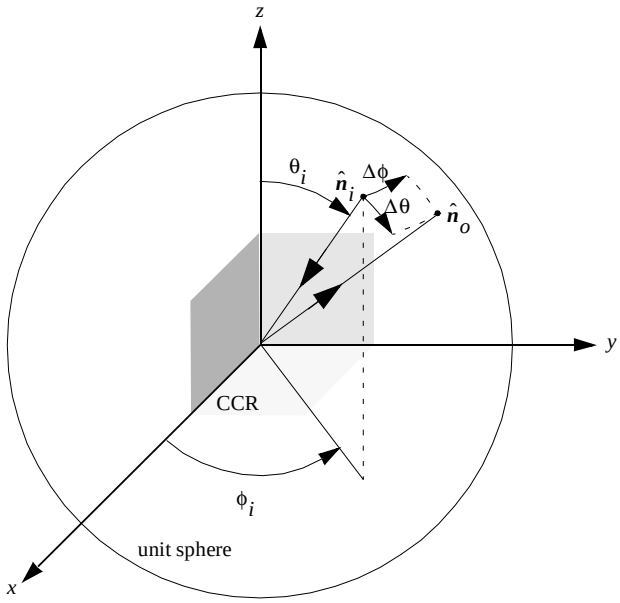

Fig. 12. Coordinate system used for simulation.

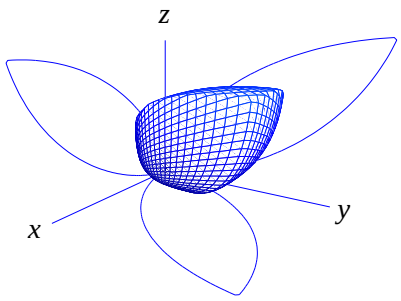

Fig. 13. Polar plot of the peak differential scattering cross section $d\sigma(\hat{\boldsymbol{n}}_i, \hat{\boldsymbol{n}}_o = \hat{\boldsymbol{n}}_i)/d\Omega_o$ for an ideal CCR.

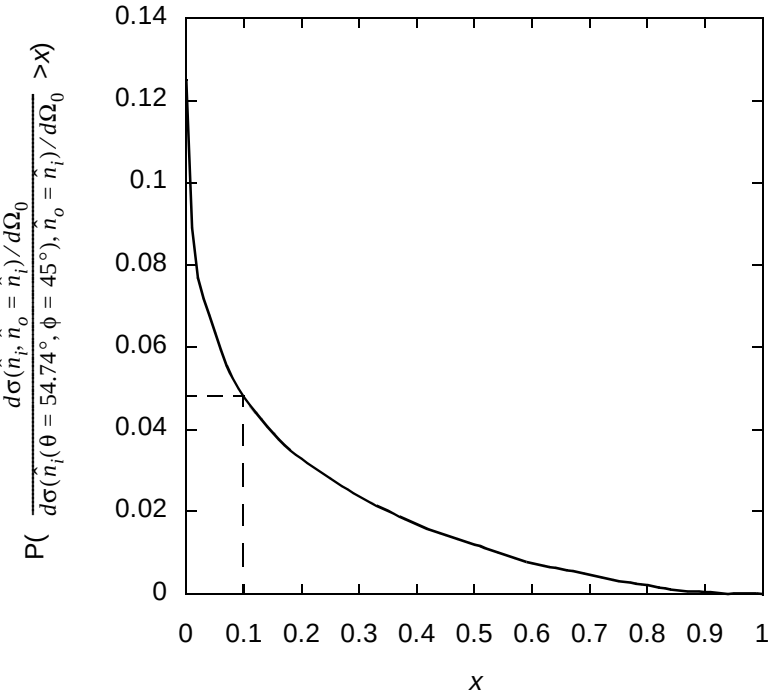

Fig. 14. Complementary cumulative distribution function of the normalized peak differential scattering cross section $(d\sigma(\hat{\boldsymbol{n}}_i, \hat{\boldsymbol{n}}_o = \hat{\boldsymbol{n}}_i)/d\Omega_o)/(d\sigma(\hat{\boldsymbol{n}}_i(\theta = 54.74°, \phi = 45°), \hat{\boldsymbol{n}}_o = \hat{\boldsymbol{n}}_i)/d\Omega_o)$ for an ideal CCR oriented randomly.

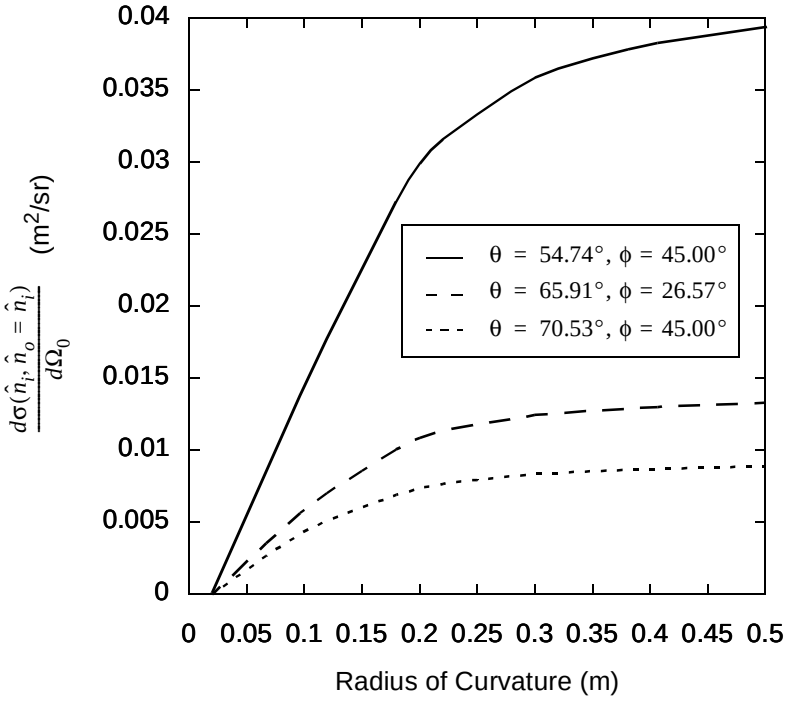

Fig. 15. Peak differential scattering cross section $d\sigma(\hat{\boldsymbol{n}}_i, \hat{\boldsymbol{n}}_o = \hat{\boldsymbol{n}}_i)/d\Omega_o$ vs. radius of curvature of CCR mirrors.

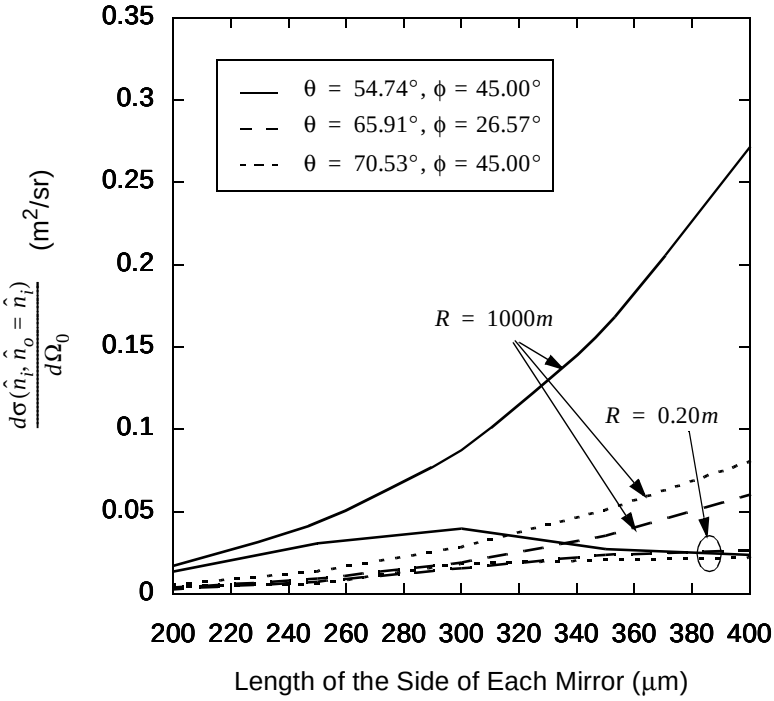

Fig. 16. Peak differential scattering cross section $d\sigma(\hat{\boldsymbol{n}}_i, \hat{\boldsymbol{n}}_o = \hat{\boldsymbol{n}}_i)/d\Omega_o$ vs. CCR size for various incident directions and radii of curvature.

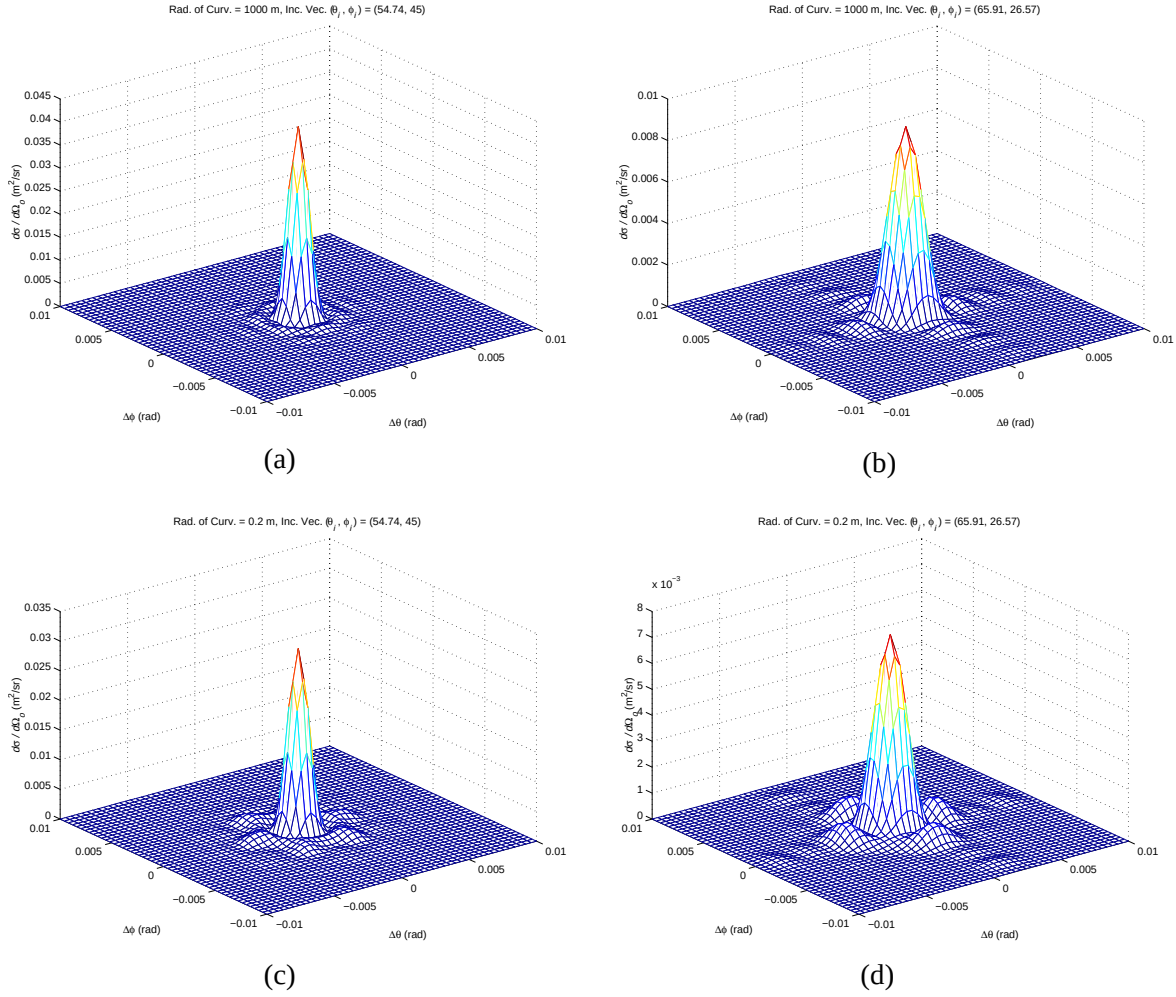

Fig. 17. Plots of differential scattering cross section $d\sigma(\hat{\boldsymbol{n}}_i, \hat{\boldsymbol{n}}_o)/d\Omega_o$ for flat and curved mirrors from different incident directions.

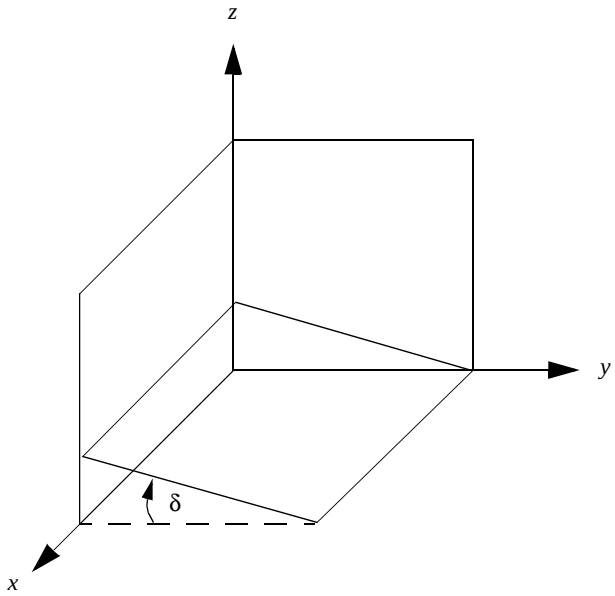

Fig. 18. Tilting the bottom mirror of the CCR.

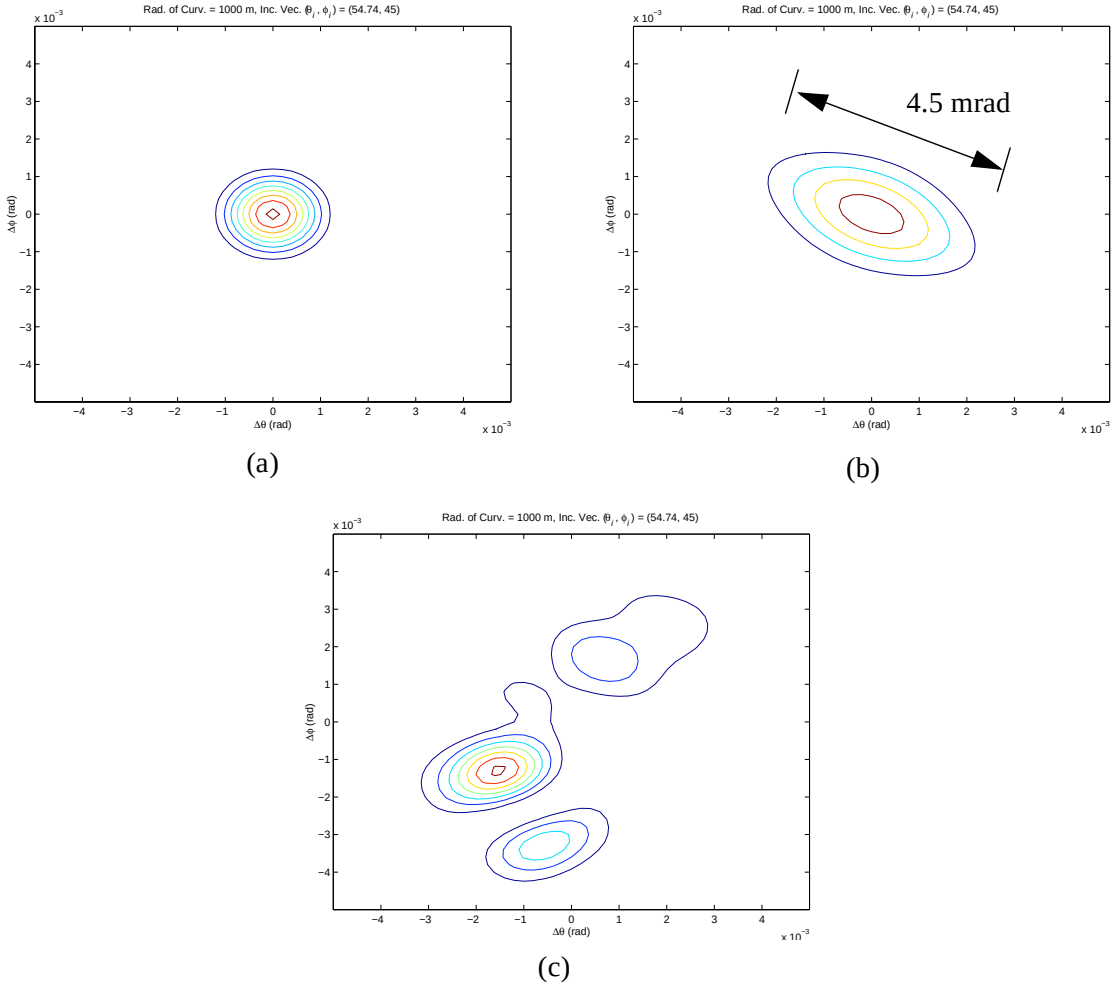

Fig. 19. Finding the minimum angular tilt and verifying with simulation. (a) Differential scattering cross section of the CCR. (b) Contribution to the differential scattering cross section from a single mirror. (c) Differential scattering cross section from the CCR with a mirror tilted 1.5 mrad.

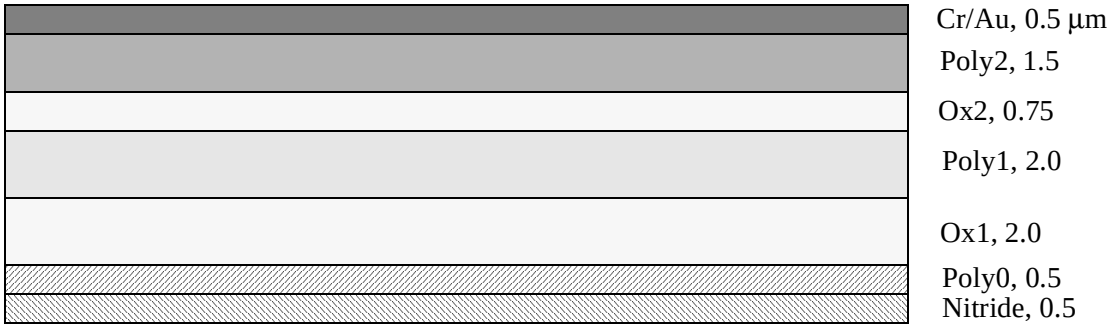

Fig. 20. MCNC MUMPS layers.

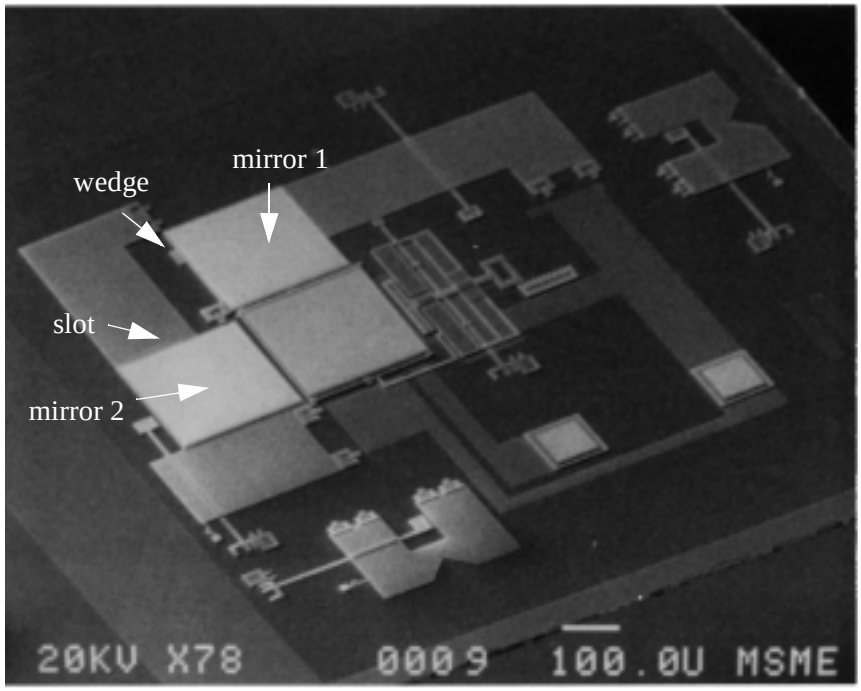

Fig. 21. A CCR that has not been assembled.

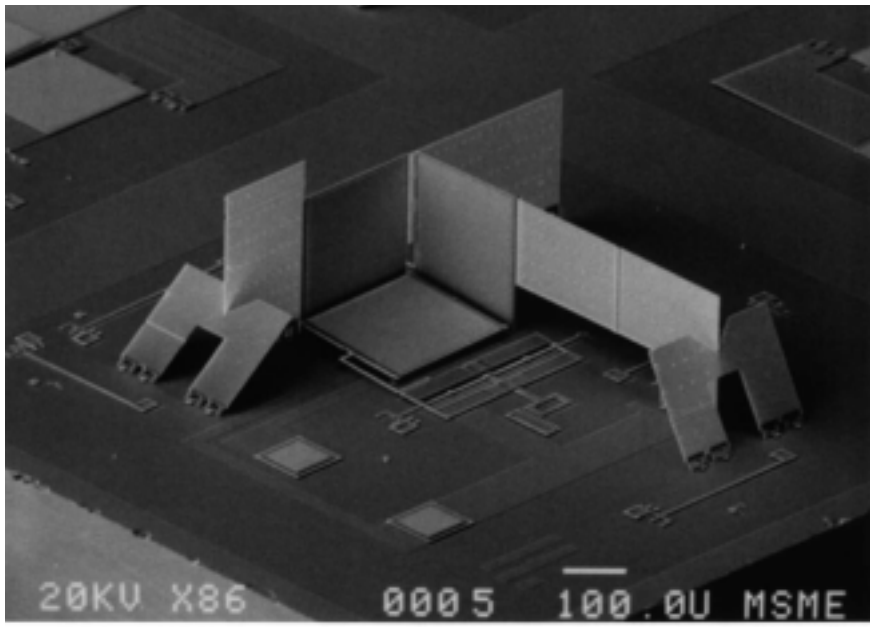

Fig. 22. An assembled CCR.

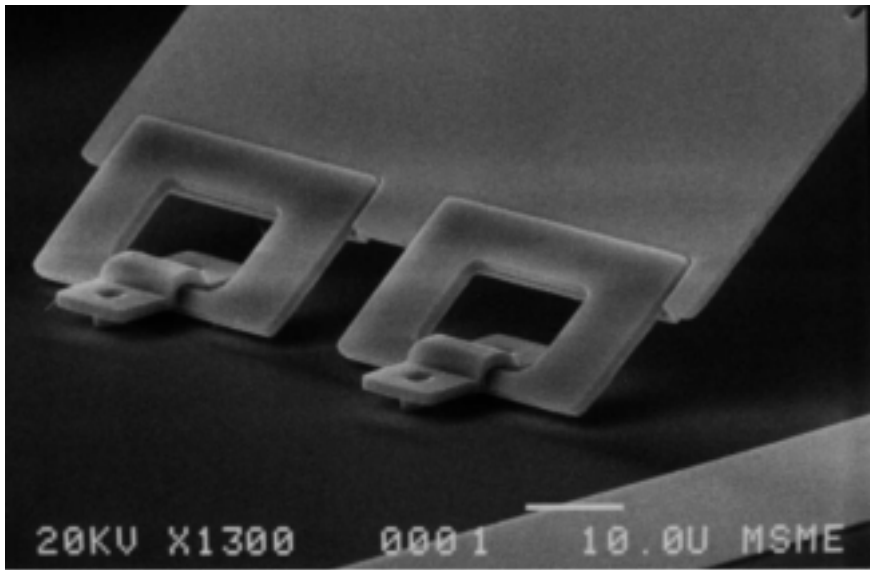

Fig. 23. MUMPS hinge.

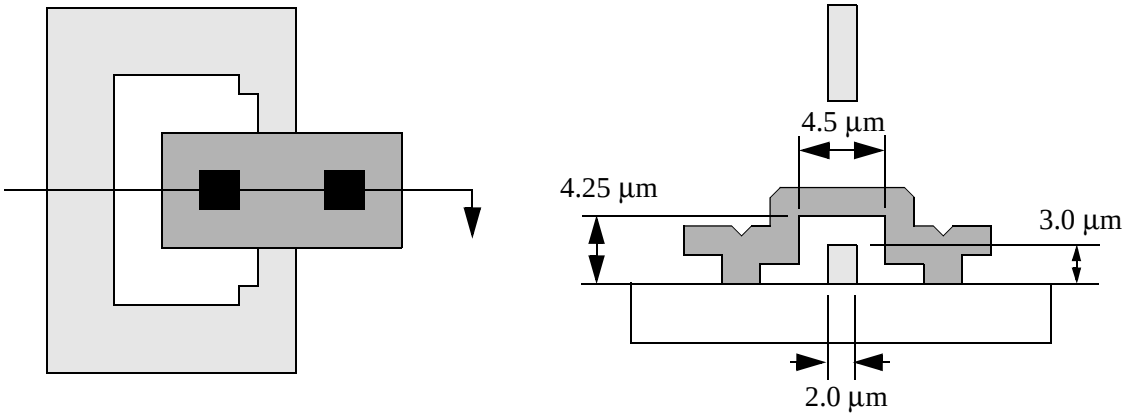

Fig. 24. Hinge layout and cross section.

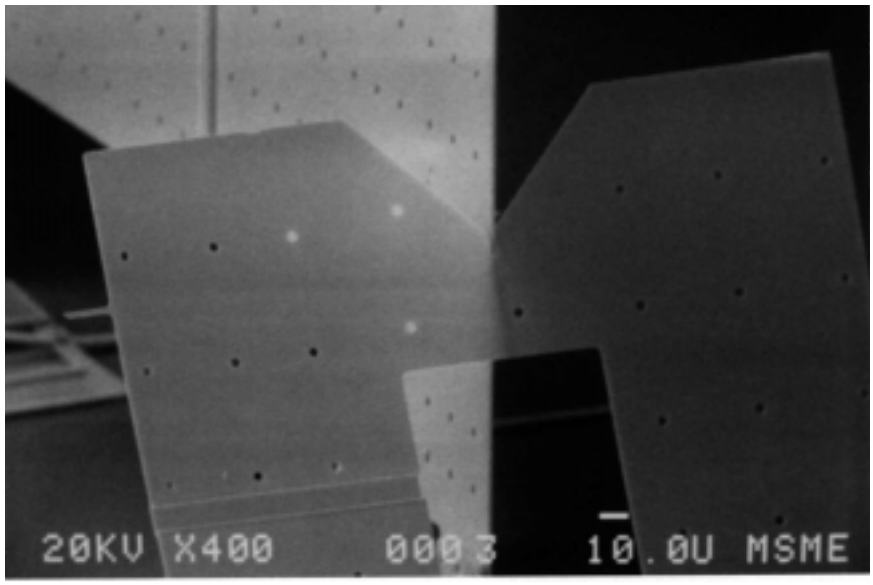

Fig. 25. Flip lock.

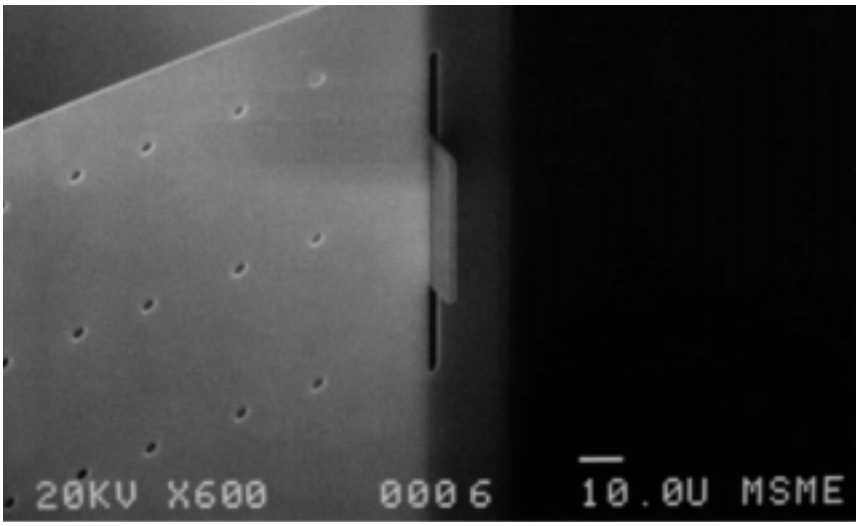

Fig. 26. Wedge in slot.

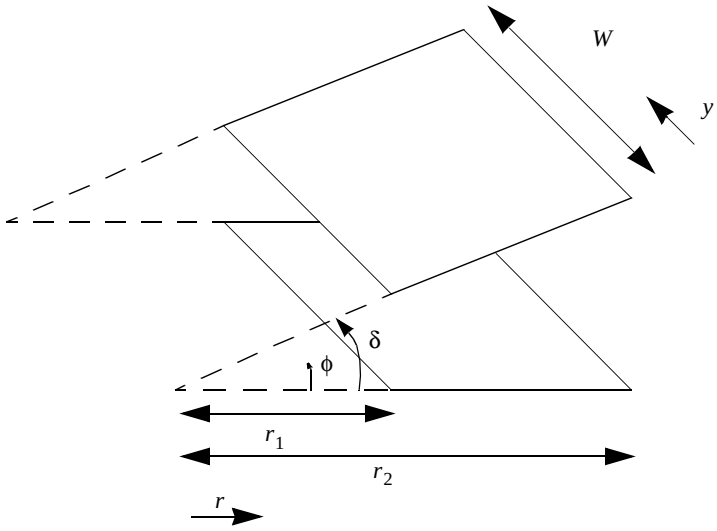

Fig. 27. Calculating the electrostatic force.

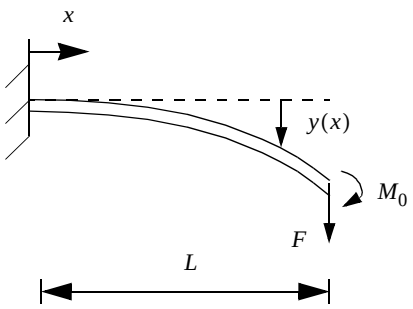

Fig. 28. Bending of a beam due to a force and moment.

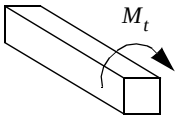

Fig. 29. Torsional bending due to a moment.

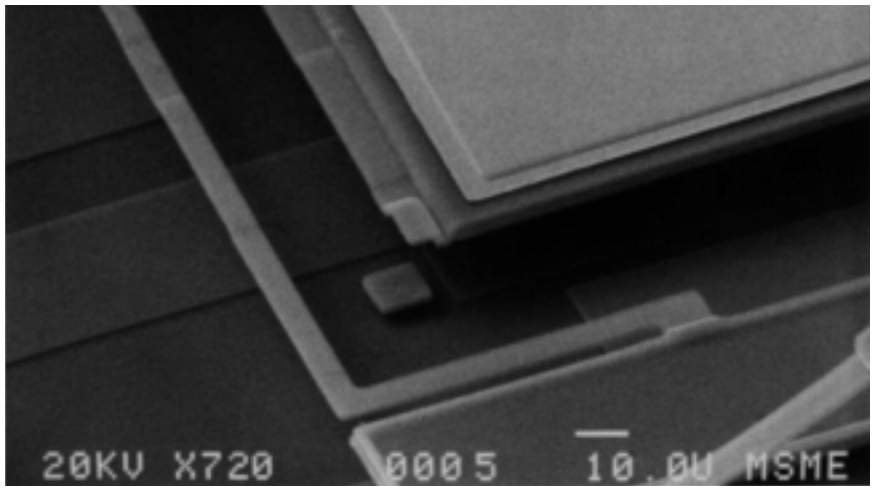

Fig. 30. Bumper.

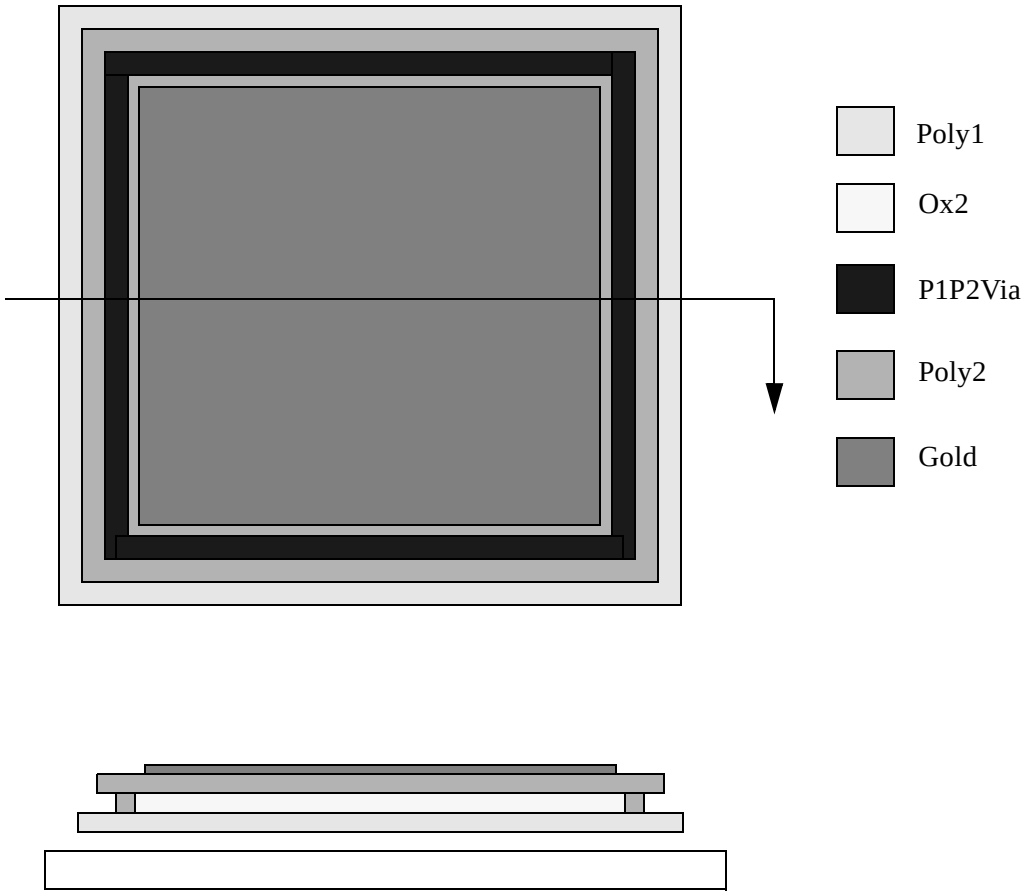

Fig. 31. Layout and cross section of a MUMPS mirror.

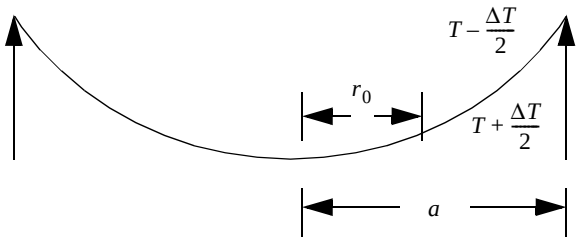

Fig. 32. Cross section of a simply supported circular plate with a uniform temperature difference ΔT between the bottom and the top surface from r_0 to a.

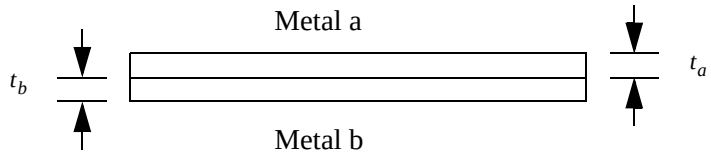

Fig. 33. Bimetallic plate.

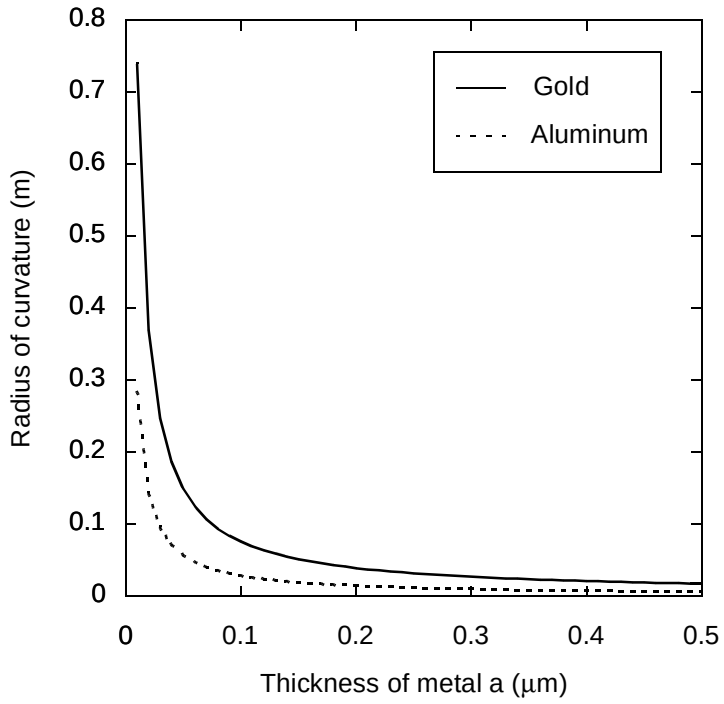

Fig. 34. Radius of curvature vs. thickness of metal a. The thickness of metal b (poly) is fixed at 3 μm.

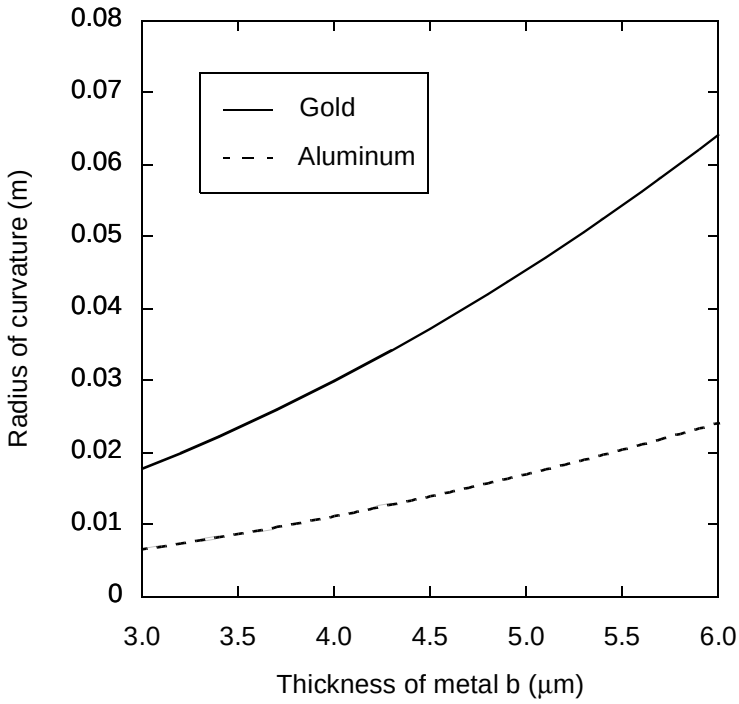

Fig. 35. Radius of curvature vs. thickness of metal b (poly). The thickness of metal a is fixed at 0.5 μm.

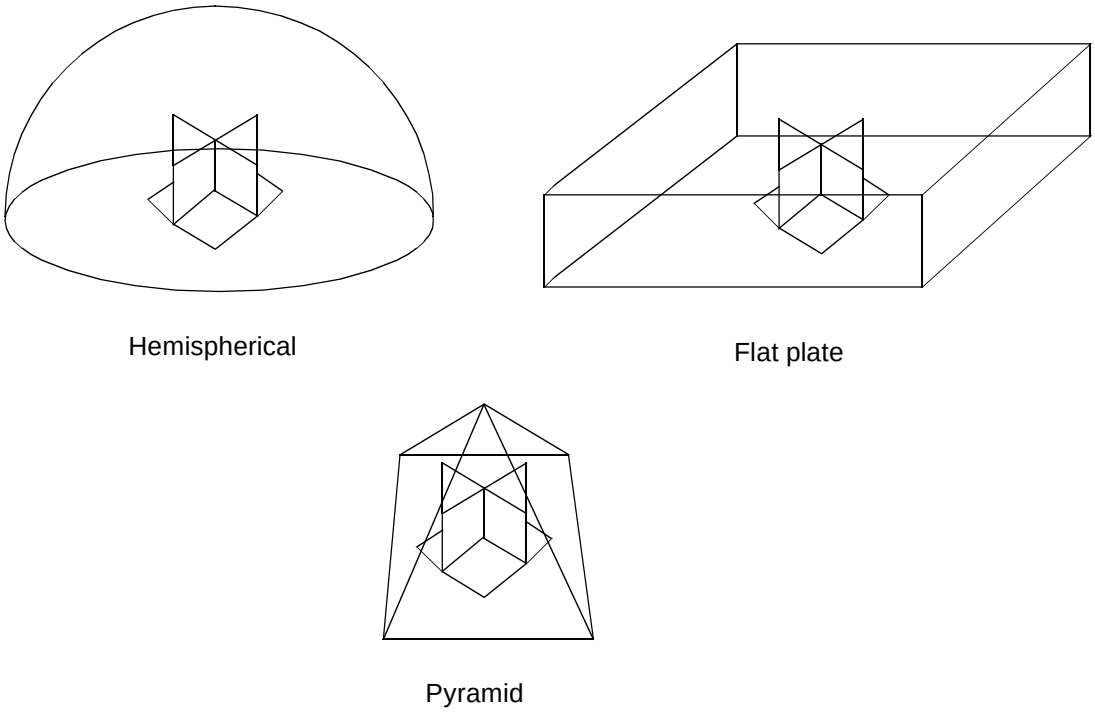

Fig. 36. Packaging options.

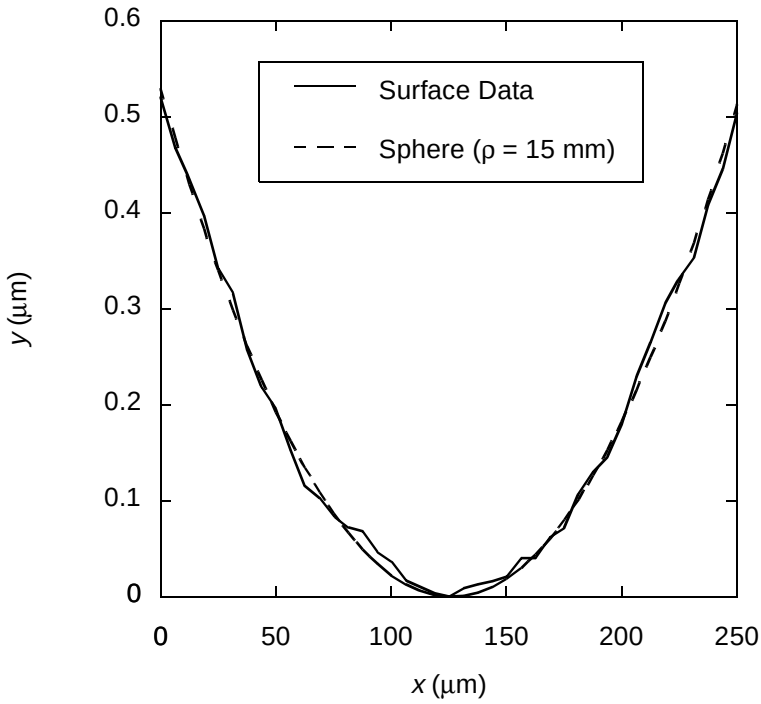

Fig. 37. Surface cross section of a MUMPS mirror.

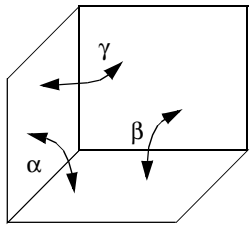

Fig. 38. Notation for misalignment data.

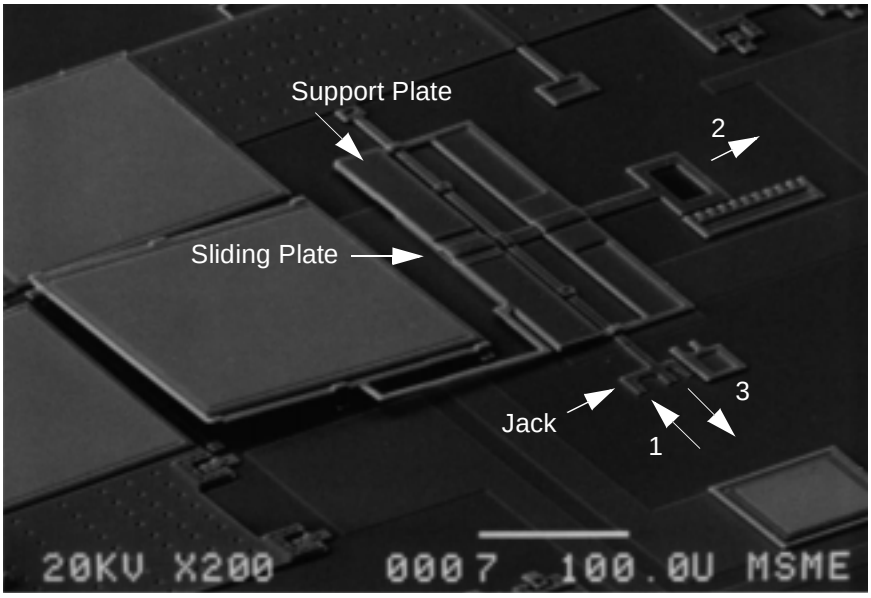

Fig. 39. Process of tilting the mirror.

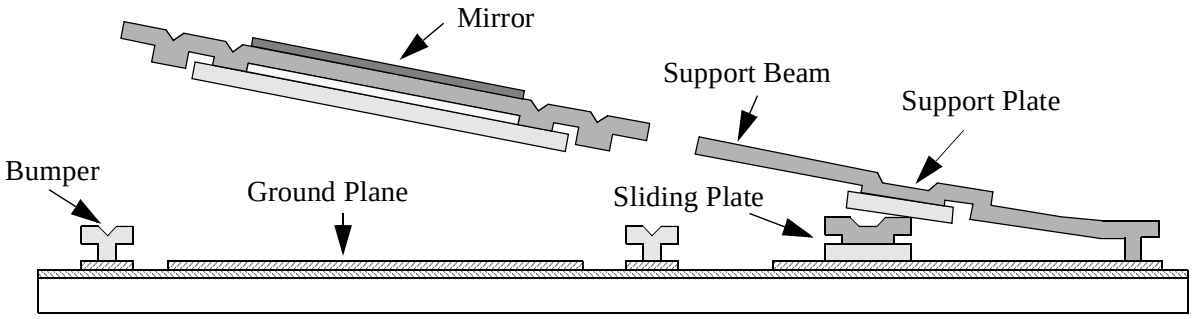

Fig. 40. Cross section of the actuator.

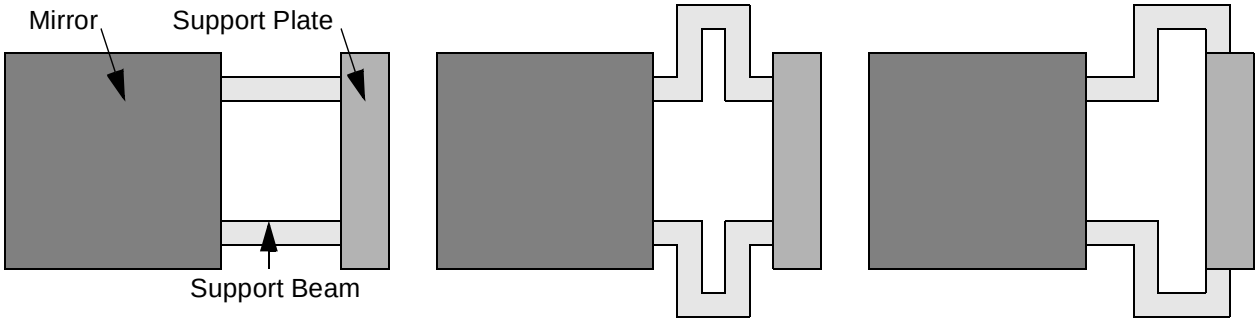

Fig. 41. Some of the support beam designs that were tested.

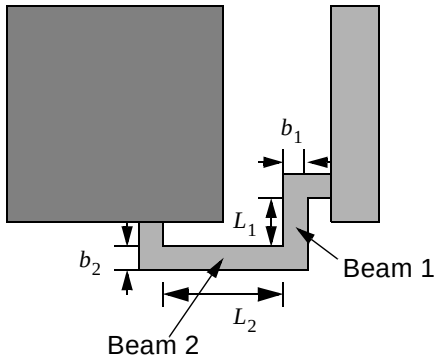

Fig. 42. Best support beam design.

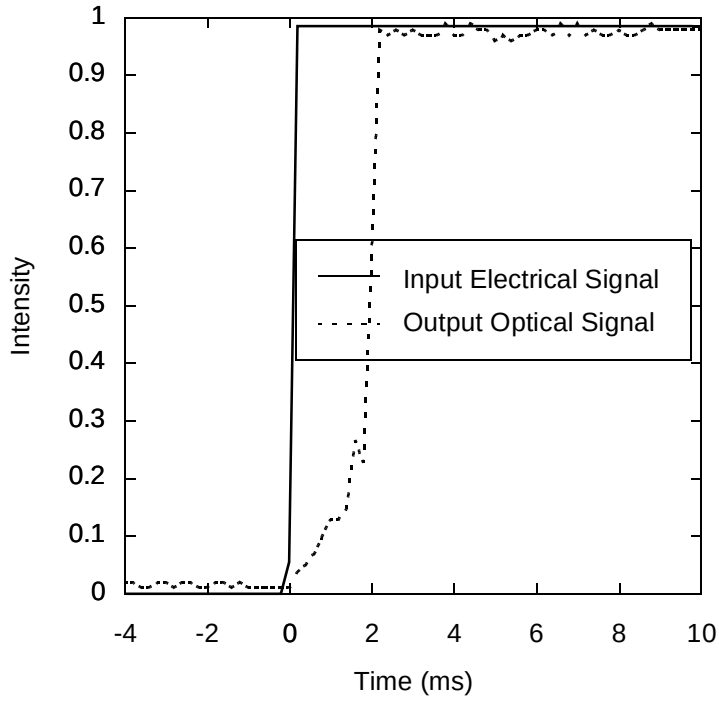

(a)

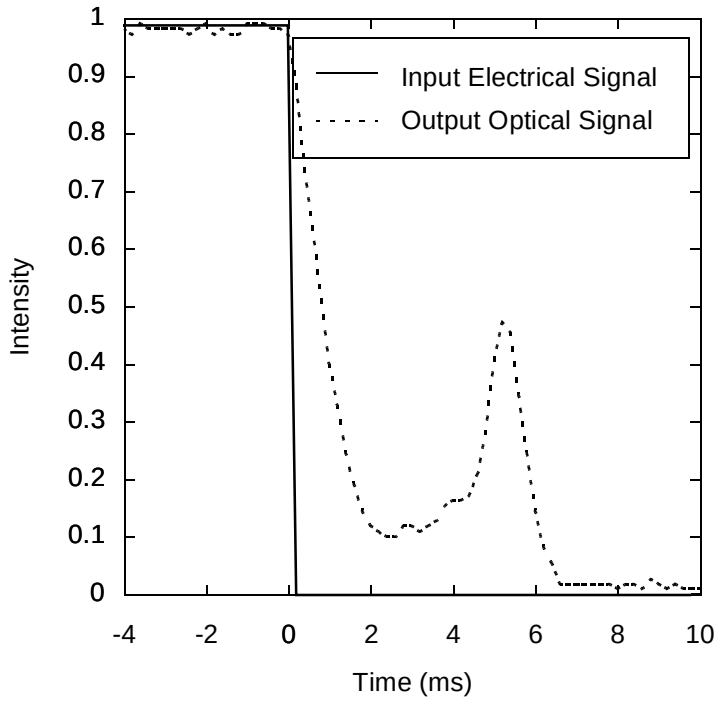

(b)

Fig. 43. CCR switching characteristics: (a) turn-on, (b) turn-off.

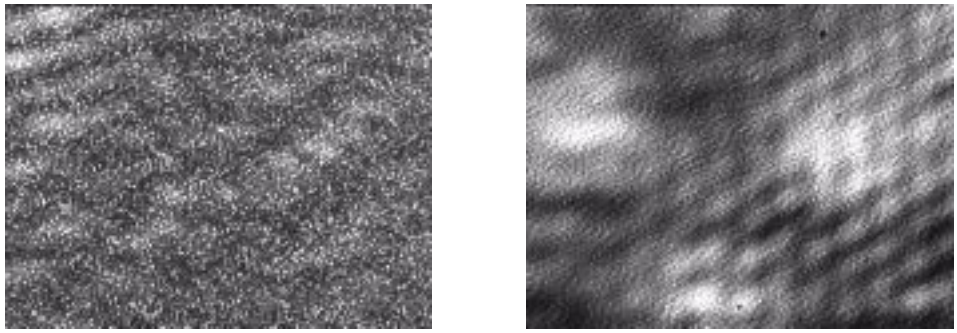

CCR Off CCR On

Fig. 44. Far-field images of light reflected from a CCR in its off and on states.

CCR Off CCR On

Fig. 45. Images captured by a video camera of the light reflected from a CCR in its off and on states.